



Contents lists available at ScienceDirect

Geochimica et Cosmochimica Acta

journal homepage: www.elsevier.com/locate/gca

The role and fate of organic carbon during aging of ferrihydrite

Yao Zhao*, Oliver W. Moore, Ke-Qing Xiao, Lisa Curti, Alba Otero Fariña, Steven A. Banwart, Caroline L. Peacock

School of Earth & Environment, University of Leeds, Leeds LS2 9JT, UK



ARTICLE INFO

Article history:

Received 21 September 2021

Accepted 3 July 2022

Available online 8 July 2022

Associate editor: Hailiang Dong

Keywords:

Iron (oxyhydr)oxides

Iron (hydr)oxides

Iron oxides

Organic matter

Organic carbon

Carboxyl

Binding strength

Aging

Dissolution recrystallisation

Mobility

ABSTRACT

The persistence of organic carbon (OC) in natural environments is widely attributed to mineral protection, especially by iron (Fe) (oxyhydr)oxides. The effect of OC binding strength on the aging of Fe (oxyhydr)oxides and the mobility and fate of OC during aging however, is unknown. Here we investigate how OC binding strength controls the aging of ferrihydrite (Fh) and subsequent retention or release of the associated OC. We focus on carboxyl-rich OC coprecipitated with Fh and track the physicochemical properties and OC stability as a function of carboxyl-richness over time. In agreement with previous work we find that during carboxyl-rich OC coprecipitation with Fh, OC is adsorbed to the Fh particle surfaces and that increasing carboxyl-richness results in an increasing number of carboxylate-Fe bonds between the OC and the mineral particles and thus increasing OC binding strength. We show that OC substantially retards the aging of Fe (oxyhydr)oxide from Fh to more crystalline Fe minerals and that this retardation increases with increasing OC binding strength. We also show that the total amount of OC decreases during aging and that the proportion of the remaining OC that is non-desorbable with 0.1 M NaOH decreases during aging for OC with relatively low binding strength but increases during aging for OC with relatively high binding strength. Our results therefore indicate that OC with higher binding strength coprecipitated with Fh becomes proportionally more stable with the solid phase and thus less mobile during aging in natural environments. We suggest that our work might offer a deeper mechanistic insight into the processes responsible for OC persistence with minerals and thus the long-term preservation of OC in natural environments.

© 2022 The Authors. Published by Elsevier Ltd. This is an open access article under the CC BY license (<http://creativecommons.org/licenses/by/4.0/>).

1. Introduction

Soils are the largest terrestrial reservoir and third largest global reservoir for organic carbon (OC) and are thus a significant component of the global carbon cycle (Jobbágy and Jackson, 2000; Ruddiman, 2001). Soil organic carbon (SOC) also improves soil structure and function, and thus contributes to a wealth of soil ecosystem services (Sparks, 2003). The composition of SOC is a subject of significant research but the OC stored in soils typically comprises a variety of plant- and microbially-derived organic components, and thus includes soil biomass and organic exudates and residues, and humic substances (humins, humic acid and fulvic acid) and non-humic substances (e.g. amino acids, carbohydrates), which although often at low abundance are highly reactive and can pronouncedly influence soil chemistry (Sparks, 2003). Together with organic nitrogen (N), phosphorus (P) and other organic building blocks, SOC forms part of soil organic matter (SOM), which is

often conceived as a continuum of progressively decomposing organic compounds that are initially derived from biomolecules (Lehmann and Kleber, 2015). Given the lability of most biomolecules, SOM should readily turn over (Lehmann and Kleber, 2015), however some SOM persists for months to millennia, which is difficult to explain from a thermodynamic perspective (Schmidt et al., 2011).

There are several hypotheses that try to explain how plant- and microbially-derived OC is stored in soils and sediments, that range from storage being due to an inherent recalcitrance of specific types of OC, which leads to their selective preservation (like lignin and cellulose) (Burdige, 2007; Hatcher et al., 1983; Hedges et al., 1985; Kellerman et al., 2015), to the protection of a range of different OC moieties from microbial degradation through their association with mineral particles (Burdige, 2007; Rothman and Forney, 2007; Six et al., 2002; Torn et al., 1997; Vogel et al., 2014). Long residence times of SOC are frequently attributed to the association of organic species with minerals, especially iron (Fe) (oxyhydr)oxides, which can stabilise SOC against microbial degradation under both oxic and anoxic conditions (Hemingway et al., 2019; Kaiser

* Corresponding author.

E-mail address: eezy@leeds.ac.uk (Y. Zhao).

and Guggenberger, 2007; Li et al., 2020; Mikutta et al., 2006; Newcomb et al., 2017; Torn et al., 1997; Zhao et al., 2016). The association of OC with minerals typically occurs through a variety of sequestration processes that remove OC from solution to the solid mineral particles (Sposito, 2008). Sequestration processes can include the surface sorption, or adsorption, of OC to preformed mineral particles and also the coprecipitation of OC with neoformed mineral phases, where OC is removed from solution as a consequence of mineral precipitation (Eusterhues et al., 2011). During coprecipitation OC can become adsorbed at mineral particle surfaces and incorporated into particle interiors, for example by being occluded into mineral pore spaces (Eusterhues et al., 2011). An important proportion (up to 40%) of total SOM in various soils is reportedly bound with reactive Fe minerals, most likely during coprecipitation (Wagai and Mayer, 2007; Zhao et al., 2016). Recent research highlights however, that the relationship between OC and Fe minerals, and thus the protection of OC from microbial degradation, is complex and influenced by soil redox and microbial activity. Reducing conditions can lead to the reductive dissolution of Fe minerals and drive carbon solubilisation, depolymerisation and loss as CO₂ (Chen et al., 2020). Microbial activity can also play a finely balanced role in OC remineralisation, which influences the functional role of Fe in OC cycling (Li et al., 2020). If microbial activity is high, the role of Fe can change from that of a sorbent to an electron acceptor, thus increasing the accessibility of OC to microorganisms (Li et al., 2020). Overall it is clear that the interactions between SOC and Fe minerals in all soil conditions can influence the long-term storage of OC in soils and regulate the global biogeochemical cycling of carbon (Adhikari et al., 2017).

Of the naturally occurring Fe minerals the (oxyhydr)oxide ferrihydrite (Fh) is common in soils and has high surface area with high surface reactivity (Hiemstra, 2013; Larsen and Postma, 2001; Michel et al., 2007). It therefore possesses an extremely high capacity to sequester OC compared to more crystalline Fe minerals (Adhikari et al., 2017; Chen et al., 2014; Kaiser and Guggenberger, 2007). Authigenic Fh is metastable under oxic conditions however, and ages to more crystalline Fe minerals, like goethite (Gt) and hematite (Hm), over time (Das et al., 2011). Because aging involves dissolution, precipitation, aggregation, sorption and desorption (Sakakibara et al., 2019) and the more crystalline Fe minerals also have different physical and chemical properties compared to Fh (Cornell and Schwertmann, 2003), the aging of Fe (oxyhydr)oxide can either enhance the mobility and migration, and hence the degradation, of OC in soils (Adhikari et al., 2017; Canfield et al., 1993; Chen et al., 2020; Han et al., 2019), or strengthen OC sequestration and fixation and thus lengthen the residence time of OC in these environments (Hu et al., 2020; Lu et al., 2019).

Due to the potential importance of Fe (oxyhydr)oxide aging on the mobility and fate of associated OC, there are several studies that investigate the aging of Fh in the presence of associated OC, and the behaviour of the associated OC as aging progresses. Regarding aging, the presence of OC can significantly influence the aging rate of Fh. Previous works show that OC can suppress the recrystallisation of Fh to more crystalline Fe minerals in both oxic (Hu et al., 2018) and anoxic environments (Chen et al., 2015; Eusterhues et al., 2014; Henneberry et al., 2012), but also facilitate the recrystallisation of Fh by electron shuttling under anoxic conditions (Amstaetter et al., 2012; Bhattacharyya et al., 2019; Jiang and Kappler, 2008; Lovley et al., 1996; Poggenburg et al., 2016). The presence of OC can also influence the physicochemical properties of the aging products formed, resulting in Fe minerals with more defects and greater porosity than those formed from pure Fh (Hu et al., 2020; Lu et al., 2019), which may provide an effective mechanism to sequester OC. Regarding the mobility and fate of the OC, work shows that during aging of Fh to more crystalline Fe minerals, OC may be sequestered (Hu et al., 2020;

Lu et al., 2019) or partially released from Fe (oxyhydr)oxides (Adhikari et al., 2017; Jelavić et al., 2020). Whether OC is retained or released during aging depends on several factors, including C/Fe ratio (Adhikari et al., 2017; Chen et al., 2015), whether OC is adsorbed or coprecipitated (Han et al., 2019), the structure and electron-shuttling properties of the OC (Amstaetter et al., 2012) and the crystalline structures of the mineral products (Hu et al., 2020; Lu et al., 2019). Despite these studies however, the effects of different types and binding strengths of OC on the aging of Fh to more crystalline Fe minerals and the mobility and fate of OC are still unknown.

One of the most important types of OC for Fe mineral-OC associations is carboxyl-rich OC. Carboxyl functional groups are prevalent in natural OC (Rothe et al., 2000) and are highly reactive towards different metal ions and mineral surfaces (Rowley et al., 2017). Because of this they play a dominant role in OC sequestration mechanisms and thus in the long-term accumulation of OC in soil (Kramer et al., 2012). Spectroscopic studies using Fourier-transform infrared spectroscopy (FTIR) and near edge X-ray absorption fine structure spectroscopy (NEXAFS) provide direct evidence for carboxylate-Fe bonds forming via a ligand exchange mechanism between carboxyl functional groups and Fe minerals (Chen et al., 2014; Chorover and Amistadi, 2001; Curti et al., 2021; Gu et al., 1994; Hall et al., 2020; Kaiser and Guggenberger, 2007; Kaiser et al., 1997; Lv et al., 2016; Solomon et al., 2005; Zeng et al., 2020). Recent NEXAFS spectroscopy however, also shows that as the number of carboxyl functional groups present in simple carboxylic OC compounds increases, the number of carboxylate-Fe bonds formed between the carboxyl functional groups and the Fh particles increases, and thus the binding strength, stability and persistence of the OC associated with Fh also increases (Curti et al., 2021).

Here we investigate how OC binding strength controls the aging of Fh and subsequent retention or release of the associated OC. We focus on carboxyl-rich OC and we use simple mono-, di- and tri-carboxylic acids with either one, two or three carboxyl functional groups and thus increasing carboxyl-richness as model carboxyl-rich compounds. We assess binding strength by determining the number of carboxylate-Fe bonds formed between the carboxyl functional groups and the Fh particles. We synthesise Fh organomineral coprecipitates and use X-ray diffraction (XRD) to confirm the mineralogy of the coprecipitates, and scanning transmission X-ray microscopy (STXM) coupled with NEXAFS, together with thermodynamic surface complexation modelling, to determine the binding strength and distribution of OC with the coprecipitates. We then subject our Fh coprecipitates to aging experiments at 75 °C to observe how the presence of the OC influences the chemical reactivity of Fe (oxyhydr)oxide during acid extraction as an operationally defined measure of crystallinity, and how the total amount of OC and the non-desorbable amount of OC changes as a function of carboxyl-richness. Our primary objectives were to (1) investigate the influence of carboxyl-rich OC with different binding strengths on the aging of Fh organominerals; (2) investigate the influence of carboxyl-rich OC with different binding strengths on the mobility and fate of OC during aging of Fh organominerals; and (3) use our results to suggest whether OC binding strength to Fh might significantly affect the stabilisation and preservation of OC in natural environments.

2. Materials and methods

2.1. Preparation of Fh organomineral coprecipitates

Eight Fh organomineral coprecipitates with different wt%C were prepared with three simple carboxylic acids following the method

of Curti et al. (2021). The acids were denoted as acid n/m , where acid refers to the first three letters of the acid IUPAC name and n/m denotes the number of carboxyl groups (n) and the number of total carbon atoms (m). The acids used were pentanoic acid (Pen1/5), hexanedioic acid (Hex2/6) and butane 1, 2, 4 tricarboxylic acid (But3/7), which have one, two and three carboxyl functional groups, respectively. Briefly, 0.1 M $\text{Fe}(\text{NO}_3)_3 \cdot 9\text{H}_2\text{O}$ (aq) solutions were mixed with varying amounts of organic acids and then the pH values of the solutions were adjusted to ~ 7 with 1 M KOH, whereupon the acids coprecipitated with the Fh, forming Fh organomineral coprecipitates with different wt% C sorbed. Fh organomineral coprecipitates were washed several times over a week in equivalent volumes of 18.2 M Ω -cm MilliQ water, after which coprecipitates were stored as a slurry at 4 °C, and part of the coprecipitates was freeze-dried for further analysis. The amounts of organic acids were varied taking into account the solubility of the acids in solution and their affinity for Fh during coprecipitation. For Pen1/5 solubility and affinity are low and constrain the maximum carbon sequestration to ~ 1 wt% C, while for Hex2/6 and But3/7 affinity is higher and allows maximum sequestration of at least ~ 7 wt% C (Curti et al., 2021). Pure ferrihydrite (Fh) as 2-line Fh was prepared via hydrolysis of a Fe(III) salt solution following the method of Schwertmann and Cornell (2000). Briefly, Fh was prepared by rapid hydrolysis of 0.1 M $\text{Fe}(\text{NO}_3)_3 \cdot 9\text{H}_2\text{O}$ (aq) with 1 M KOH at pH 7. Fh was washed several times over a week in equivalent volumes of 18.2 M Ω -cm MilliQ water, after which Fh was stored as a slurry at 4 °C (Schwertmann and Cornell, 2000). Plastic labware and AR grade reagents were used throughout the preparations.

The C contents of the solids were determined on solid freeze-dried subsamples using LECO SC-144DR Dual Range Sulphur and Carbon Analyzer. The Fe contents of the solids were determined after total digestion using 6 mol L⁻¹ HCl on an Atomic Absorption Spectrophotometer (iCE 3300 AAS). Eight coprecipitates were obtained: Fh-pentanoic acid with 1.2 wt% C and C:Fe molar ratio 0.098 (Fh_Pen1/5_1.2 wt% C); Fh-hexanedioic acid with 2.9 wt% C and C:Fe molar ratio 0.246 (Fh_Hex2/6_2.9 wt% C), 4.1 wt% C and C:Fe molar ratio 0.358 (Fh_Hex2/6_4.1 wt% C), 4.5 wt% C and C:Fe molar ratio 0.396 (Fh_Hex2/6_4.5 wt% C), and 7.0 wt% C and C:Fe molar ratio 0.652 (Fh_Hex2/6_7.0 wt% C); and Fh-butane 1, 2, 4 tricarboxylic acid with 6.0 wt% C and C:Fe molar ratio 0.555 (Fh_Fh_But3/7_6.0 wt% C), 7.3 wt% C and C:Fe molar ratio 0.699 (Fh_But3/7_7.3 wt% C), and 7.8 wt% C and C:Fe molar ratio 0.757 (Fh_Fh_But3/7_7.8 wt% C).

2.2. Characterisation of Fh organomineral coprecipitates

2.2.1. X-ray diffraction and scanning transmission X-ray microscopy near-edge X-ray absorption fine structure spectroscopy

The mineralogy of the Fh coprecipitates and pure Fh prior to aging was confirmed on freeze-dried subsamples via X-ray diffraction (XRD) using a Bruker D8 Diffractometer with Cu-K α radiation ($\lambda \approx 0.154$ nm). Diffractograms were recorded from 2 to 90° 2 θ with 0.02° 2 θ step size and 930 ms acquisition time. Silicon dioxide was used as an analytical standard.

The binding strength of the OC to Fh in the Fh coprecipitates and the distribution of OC with the Fh coprecipitate particles prior to aging were investigated directly using STXM NEXAFS. The C 1 s STXM NEXAFS for the Fh coprecipitates was recorded on Beamline I08, Diamond Light Source Ltd, Oxfordshire, UK, following the method of Curti et al. (2021). Briefly, for analysis ~ 5 mg of freeze-dried subsample was suspended in ~ 500 μL of 18.2 M Ω -cm MilliQ water and then an aliquot of ~ 5 μL of suspension was pipetted onto a glow-discharged Si₃-N₄ membrane window (Silson Ltd) and left to air dry. Stacked data sets for C were collected from 275 to 310 eV, using varied energy resolution across different spectral

regions of 0.5, 0.1 and 0.2 eV step size for pre-edge, running up to and over the edge, and post-edge, respectively. To minimise beam damage on the sample, dwell times were set to 10 ms per energy step based on beam damage tests conducted by repeatedly measuring the same area of sacrificial samples. The unreacted acids were analysed as unmodified acid solids or liquids as applicable. X-ray absorption stacks were aligned using the Axis2000 software. The NEXAFS spectra were extracted from individual coprecipitate particles and the dark signal was subtracted from the raw data using the Mantis software. The NEXAFS spectra were then exported for baseline correction, alignment, calibration and normalisation using the Athena software (Ravel and Newville, 2005). Baseline correction and normalisation avoid spectral dependence on the total C content, and spectral features and peak shifts are thus indicative of C molecular structure and chemistry and not C concentration effects occurring during NEXAFS measurement. Peak identification was done with reference to literature assignments. The STXM images were used to show the spatial correlation between C and Fe, again following the method of Curti et al. (2021). Briefly, C and Fe elemental distribution maps were created by aligning and then converting C and Fe images to optical density (OD) using the transmitted flux through the sample (I) and the incident flux measured in an empty region adjacent to the analysed particles (I_0) where $\text{OD} = \ln(I_0/I)$. Distribution maps for C and Fe were taken on the same region and with the same number of pixels and were then aligned to common reference features and overlapped. To determine the C-Fe correlation coefficients, elemental thickness values on a pixel-by-pixel basis were compared by extracting the OD values using the Axis 2000 software, saved as an ASCII file, and then the OD values for both C and Fe stacks were plotted against one another. The energies for obtaining the C and Fe distribution maps were C 1 s 282.0–289.0 eV and Fe 2p 705.0–712.0 eV.

2.2.2. Thermodynamic surface complexation modelling

The binding strength of the OC to Fh in the Fh coprecipitates prior to aging was also investigated indirectly by measuring the adsorption of Pen1/5, Hex2/6 and But3/7 to pure Fh in batch adsorption pH edge experiments and then using a thermodynamic surface complexation model to constrain the binding affinity of these acids. Batch adsorption experiments of the acids on pure Fh were prepared from pH 3.5 to 10.0. Pure Fh mineral slurry was added into 18.2 M Ω -cm MilliQ water and either Pen1/5, Hex2/6 and But3/7 stock solutions were added to give a total volume of 45 mL, a solid solution ratio of 2 g dry sorbent L⁻¹ and OC concentrations of 0.4 mM in 0.01 M NaNO₃ background electrolyte. After addition of stock solution, pH of the resulting suspensions was adjusted by dropwise addition of either dilute HNO₃ or NaOH. After shaking continuously for 48 h, the suspensions were filtered with 0.22 μm cellulose nitrate filters using a vacuum filtration apparatus and the solids were collected and rinsed with 15 mL DI water to remove aqueous OC. The solids were then freeze-dried. The total C contents of the solids were determined using a LECO SC-144DR Dual Range Sulphur and Carbon Analyzer. The amount of OC sorbed was calculated by subtracting the amount of C present for pure Fh (the control). The calculated OC sorbed (wt% C) and the dry sorbent concentration (2 g/L) were then used to calculate the molar concentration of OC adsorbed. All adsorption experiments were conducted in duplicate.

Following the successful application of the diffuse double layer model and triple layer model to simulate the adsorption of simple organic acids on Gt (Evanko and Dzombak, 1999; Mesuere and Fish, 1992a,b), the adsorption behavior of the carboxylic acids on Fh was fit to a thermodynamic surface complexation model using the program EQLFOR (Sherman et al., 2008). The basic Stern model (BSM) (Westall and Hohl, 1980) was used to account for the surface

electrostatics in the Fh system with a 3-site 1 pK formalism for protonation of the Fh surface, involving two types of singly-coordinated surface oxygens (edge-sharing $\equiv\text{FeOH}_c^{-0.5}$ and corner-sharing $\equiv\text{FeOH}_c^{-0.5}$) and the triply-coordinated oxygens ($\equiv\text{Fe}_3\text{O}^{-0.5}$) (Hiemstra and Van Riemsdijk, 2009; Hiemstra et al., 1989; Hiemstra et al., 1996). The model input parameters for the binding constants for protonation of the surface functional groups, binding constants for electrolyte ions associating with these groups, site densities of the groups and capacitance of the Stern layer have been constrained for Fh in previous work (Moon and Peacock, 2013). The binding constants for protonation of the carboxylic acid groups have also been constrained in previous work (Dean, 1987) or were calculated for this study using the ACD/I-Lab 2.0 software (ACD/I-Lab, version 2.0, Advanced Chemistry Development, Inc). The specific surface area (SSA) of the Fh was determined by the multi-point BET (Brunauer, Emmett and Teller) technique using a Micromeritics Gemini VII 2390a Surface Area Analyser, with samples dried and degassed at room temperature for 24 h using N_2 (g) (<1 ppm CO_2 (g)) prior to analysis. All SSA analyses were performed in triplicate.

2.3. Aging of Fh organomineral coprecipitates

After preparation and characterisation of the Fh coprecipitates, Fh coprecipitate slurries and pure Fh were added into 0.01 M NaNO_3 background electrolyte to produce 2 g/L suspensions, and then adjusted to target pH values with dilute HNO_3 or NaOH . The pH values were buffered at pH 5 and 6.5 by adding 30 mmol/L organic buffer 2-(N-Morpholino)ethane-sulphonic acid (MES) and 3-(N-Morpholino) propanesulphonic acid (MOPS), respectively. These buffer solutions are negligibly sequestered to Fh (see Supplementary Information) and have been shown to have a negligible impact on the recrystallisation of Fh to more crystalline Fe minerals during aging (Bradbury and Baeyens, 1999; Ford et al., 1999). The resultant solutions were then transferred to an electric oven kept at a temperature of 75 °C for 19 days. During aging, the vessels were gently shaken to keep the suspensions homogenised. Aliquots of the solid precipitates and solutions were collected and analysed at pre-designed time intervals to track changes in the physicochemical characteristics of the Fh coprecipitates as described below. At each sampling, the suspensions were cooled to room temperature and the pH was measured. A temperature of 75 °C was used in the aging experiments as it has been shown to accelerate the recrystallisation of Fh to more crystalline Fe minerals during aging without substantially altering the aging process from that observed at 25 °C (Das et al., 2011) or causing the decomposition of Pen1/5 (McCullom and Seewald, 2003), Hex2/6 (safety data sheet (Sigma-A26357)) and But3/7 (safety data sheet (Sigma-514101)). A 19 days reaction time was used in the aging experiments based on test experiments that determined the time necessary for no further changes in the physicochemical characteristics of the Fh coprecipitates in most reaction systems.

2.4. Measured physicochemical characteristics of Fh organomineral coprecipitates during aging

To investigate the recrystallisation of Fh to more crystalline Fe minerals during aging, an acid extraction method was used that quantified the proportion of the total Fe in the solid phase that was digested by 6 mol L^{-1} HCl ($[\text{Fe}(\text{T})_{6 \text{ M HCl}}]$) compared to the proportion of Fe in the solid phase that was digested by 0.4 mol L^{-1} HCl ($[\text{Fe}(\text{T})_{0.4 \text{ M HCl}}]$) (Wang et al., 2020). In this approach, the 6 mol L^{-1} HCl step has been shown to cause the total digestion of all solid Fe phases and thus represent the total concentration of all solid phase Fe minerals (Wang et al., 2020). The 0.4 mol L^{-1} HCl step has been shown to not cause the digestion of the more

crystalline Fe minerals formed during the oxic aging of Fh, like Gt (Reddy et al., 2015) and Hm (see Supplementary Information). As soluble Fe(III) in the aqueous phase was below detection limits before adding acids (Reddy et al., 2015), the concentration of Fe in the supernatant after the 0.4 mol L^{-1} HCl step thus represented the total concentration of acid-reactive solid phase Fe minerals, nominally Fh (Wang et al., 2020). Test experiments performed to determine the efficiency of extracting Fh from mixtures of Fh and Hm at 0 %, 25 %, 50 %, 75 % and 100 % Fh showed that the extraction efficiency for Fh was over 95 % (see Supplementary Information). To perform the acid extraction subsamples were collected from each batch reactor suspension for analyses of Fe concentrations. Two 1 mL aliquots from each suspension were pipetted into 2 mL centrifuge tubes. Then 1 mL 12 mol L^{-1} HCl was added into one aliquot to get 6 mol L^{-1} HCl in suspension for the determination of total Fe in the solid phase ($[\text{Fe}(\text{T})_{6 \text{ M HCl}}]$), and 1 mL 0.8 mol L^{-1} HCl was added into the other aliquot to get 0.4 mol L^{-1} HCl, reacted for 10 mins, then centrifuged, and filtered for the determination of acid-reactive Fe in the solid phase ($[\text{Fe}(\text{T})_{0.4 \text{ M HCl}}]$). The concentration of Fe was determined on an Atomic Absorption Spectrophotometer (iCE 3300 AAS). Then the fraction of remaining Fh was quantitatively calculated through the equation: $[\text{Fe}(\text{T})_{0.4 \text{ M HCl}}] / [\text{Fe}(\text{T})_{6 \text{ M HCl}}]$. All operations above were conducted at least in duplicate.

To investigate the stability of OC during the recrystallisation of Fh to more crystalline Fe minerals during aging, two 15 mL aliquots were subsampled from the reactor and filtered with 0.22 μm cellulose nitrate filters using a vacuum filtration apparatus. The mineral particles were collected and rinsed using 15 mL DI water. One of the mineral particle subsamples was freeze-dried and kept at 4 °C for total solid C measurement ($[\text{C}_{\text{total}}]$). The other mineral particle subsample was re-suspended in 15 mL 0.1 M NaOH and shaken for 24 h to extract OC from the solid (Kaiser and Guggenberger, 2000), which was operationally defined as desorbable OC ($[\text{C}_{\text{desorbable}}]$). After the 0.1 M NaOH wash the mineral particles were filtered with 0.22 μm PES filters, washed, collected, freeze-dried and kept for C measurement, which was operationally defined as non-desorbable OC ($[\text{C}_{\text{non-desorbable}}]$). The C contents of solids were determined using LECO SC-144DR Dual Range Sulphur and Carbon Analyzer. All operations above were conducted at least in duplicate.

To further investigate the physicochemical characteristics of the Fh coprecipitates as a result of aging, SSA and total pore volume (TPV) of the Fh coprecipitates and pure Fh after aging were measured. Briefly, around 100 mL suspensions after 19 days aging at pH 6.5 were centrifuged at 2750 rpm for 20 mins, and the solid minerals were treated with 0.1 M NaOH to desorb OC. After shaking for 24 h, the suspensions were centrifuged, washed and then freeze-dried for SSA measurement determined from duplicate N_2 gas adsorption–desorption isotherms recorded using a Micromeritics Gemini VII 2390a Surface Area Analyzer, with samples dried and degassed at room temperature for 24 h using N_2 (g) (<1 ppm CO_2 (g)) prior to analysis. The total pore volume was calculated from the volume of adsorbed N_2 at partial pressure $P/P_0 \sim 0.95$. The average pore radius was calculated as $r_p = 2V_{\text{liq}}/\text{SSA}$, where V_{liq} is the volume of liquid N_2 contained in the pores. All measurements were performed in duplicate.

3. Results

3.1. Characterisation of Fh organomineral coprecipitates prior to aging

The XRD pattern of selected Fh coprecipitates prior to aging is plotted in Fig. S3 and confirms that the mineralogy of the initial

Fh coprecipitates is Fh, without detectable amounts of more crystalline Fe minerals.

The NEXAFS spectra for selected Fh coprecipitates prior to aging, together with their respective unreacted acid standards, are shown in Fig. 1. In agreement with previous work for the sequestration of these acids by Fh during coprecipitation (Curti et al., 2021), the Fh coprecipitate spectra exhibit one major peak at ~288.6 eV corresponding to carboxyl C ($\pi^*C = O$, 287.7–289 eV (Curti et al., 2021)), which is reduced in amplitude and broadened, compared to the respective standard (Fig. 1). This carboxyl peak position is also shifted to lower energy, compared to the respective standard, with the shift becoming increasingly pronounced with an increasing number of carboxyl groups (shift from respective standard for Pen1/5_1.2 wt%C: -0.1 ± 0.05 eV; for Fh_Hex2/6 coprecipitates: -0.2 ± 0.05 eV; for Fh_But3/7 coprecipitates: -0.4 ± 0.05 eV) (Fig. 1). A representative STXM image of the Fh coprecipitates prior to aging is shown in Fig. S4. The STXM elemental distribution map shows that C and Fe are highly spatially correlated ($R^2 = 0.71$) (Fig. S4).

3.2. Adsorption of carboxylic acids to ferrihydrite

The adsorption of Pen1/5, Hex2/6 and But3/7 to pure Fh as a function of pH is plotted in Fig. 2. In agreement with previous studies for organic acids adsorbed on Fe (oxyhydr)oxides (Lindegren et al., 2009), all carboxylic acids show a reverse sigmoid adsorption edge with higher adsorption in the low-mid (~3.5 to ~6) pH range. Compared to Pen1/5, Hex2/6 and But3/7 show significantly higher maximum adsorption percentages and the adsorption edges, especially for But3/7, shift to higher pH.

3.3. Aging of ferrihydrite coprecipitates

3.3.1. Acid extraction of ferrihydrite coprecipitates as a function of aging time

The acid extraction data for Fh coprecipitates at pH 5 and 6.5 as the fraction of Fh remaining after extraction as a function of aging time is plotted in Fig. 3. The presence of the carboxylic acids in the coprecipitate systems results in a higher fraction of Fh remaining with reaction time compared to the pure Fh system, and thus the carboxylic acids appear to retard the aging of Fh to more crystalline

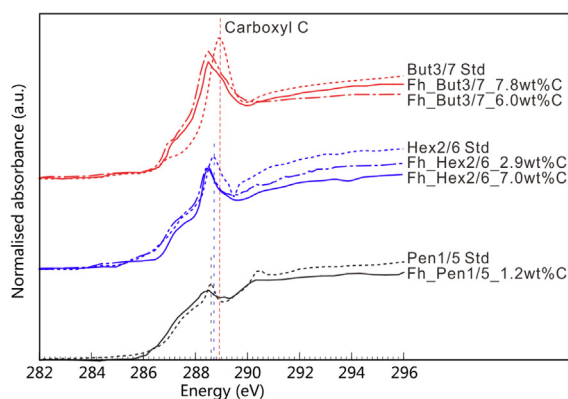


Fig. 1. Carbon 1s NEXAFS spectra for Fh_Pen1/5_1.2 wt%C and both Fh_Hex2/6 and Fh_But3/7 coprecipitates at the lower and upper end of wt%C sequestered (solid and dashed-dotted lines), together with Pen1/5, Hex2/6 and But3/7 unreacted acid standards (dotted lines). Black, blue and red colours represent Pen1/5, Hex2/6 and But3/7 data, respectively. Carboxyl C peak position for the unreacted Pen1/5, Hex2/6 and But3/7 standards are shown with vertical dashed black, blue and red lines, respectively. Spectra are stacked with an arbitrary offset for clarity. Pen1/5, Hex2/6 and But3/7 represent simple carboxyl-rich OC with one, two and three carboxyl groups, respectively. (For interpretation of the references to colour in this figure legend, the reader is referred to the web version of this article.)

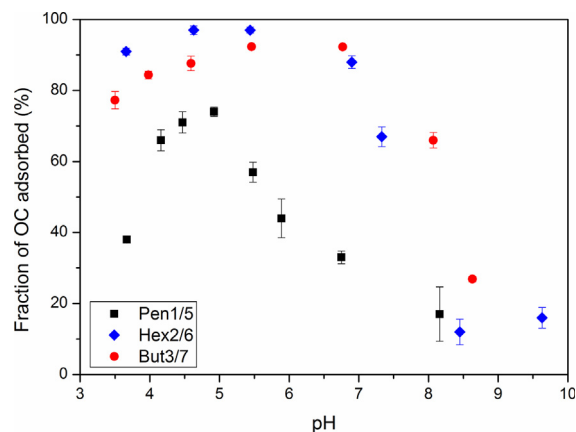


Fig. 2. OC adsorption on pure Fh as a function of pH (3.5–10). Experiments were performed with about 4×10^{-4} M OC (Pen1/5: 4.16×10^{-4} M; Hex2/6: 4.29×10^{-4} M and But3/7: 4.17×10^{-4} M) in 0.01 M NaNO₃ background electrolyte and a solid-solution ratio of 2 g dry sorbent L⁻¹. Black, blue and red symbols represent Pen1/5, Hex2/6 and But3/7 data, respectively. Pen1/5, Hex2/6 and But3/7 represent simple carboxyl-rich OC with one, two and three carboxyl groups, respectively. Error bars represent standard deviations of duplicate samples. (For interpretation of the references to colour in this figure legend, the reader is referred to the web version of this article.)

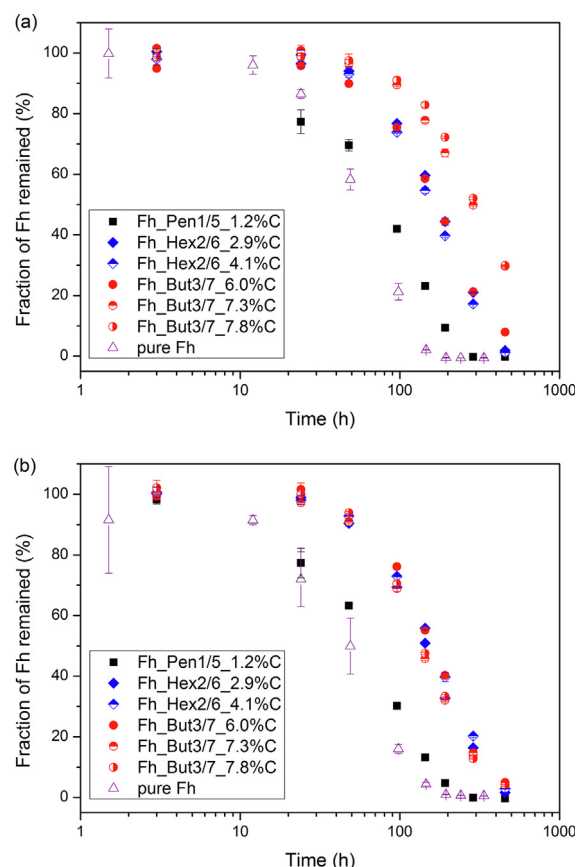


Fig. 3. Fraction of Fh remaining after acid extraction for Fh coprecipitates and pure Fh at pH 5 (a) and 6.5 (b). Experiments were performed with Fh coprecipitates in 0.01 M NaNO₃ background electrolyte and a solid-solution ratio of 2 g dry sorbent L⁻¹ at 75 °C. Black, blue and red symbols represent Pen1/5, Hex2/6 and But3/7 data, respectively. Pen1/5, Hex2/6 and But3/7 represent simple carboxyl-rich OC with one, two and three carboxyl groups, respectively. Error bars represent standard deviations of at least duplicate samples. (For interpretation of the references to colour in this figure legend, the reader is referred to the web version of this article.)

Fe minerals. This retardation appears to be a function of the number of carboxyl groups in the sequestered acid molecules and thus generally increases in the order Pen1/5 < Hex2/6 < But3/7 (at pH 5) and Pen1/5 < Hex2/6 ~ But3/7 (at pH 6.5), but this trend is complicated by the commensurate increase in the C loading of the coprecipitates with the number of carboxyl groups, so that with increased C loading retardation also generally increases. Specifically at pH 5 retardation as a function of carboxyl richness and C loading follows the order Fh_Pen1/5_1.2 wt%C < Fh_Hex2/6_2.9 % C ~ Fh_Hex2/6_4.1 %C < Fh_But3/7_6.0 %C < Fh_But3/7_7.3 %C ~ Fh_But3/7_7.8 %C. While at pH 6.5 retardation as a function of carboxyl richness and C loading is less pronounced and follows the order Fh_Pen1/5_1.2 wt%C < Fh_Hex2/6_2.9 %C ~ Fh_Hex2/6_4.1 %C ~ Fh_But3/7_6.0 %C ~ Fh_But3/7_7.3 %C ~ Fh_But3/7_7.8 %C.

3.3.2. Specific surface area and total pore volume of ferrihydrite coprecipitates after aging

The specific surface area (SSA) and total pore volume (TPV) parameters for Fh coprecipitates and pure Fh after 19 days aging at pH 6.5 are listed in Table 1. The SSA follows the order pure Fh < Fh_Pen1/5_1.2 wt%C < Fh_Hex2/6_7.0 wt%C < Fh_But3/7_7.3 wt%C, while the TPV follows the order pure Fh < Fh_Pen1/5_1.2 wt%C < Fh_But3/7_7.3 wt%C < Fh_Hex2/6_7.0 wt%C.

3.4. Carbon stability during aging of ferrihydrite coprecipitates

3.4.1. Temporal changes of total C in the solid phase

The changes in the total amount of C ($[C_{\text{total}}]$) as a function of aging time at pH 5 and 6.5 are shown in Fig. 4 and summarized in Table 2a. For Fh_Pen1/5 the $[C_{\text{total}}]$ at pH 5 and 6.5 is invariant with aging time. For Fh_Hex2/6 and Fh_But3/7 however, the $[C_{\text{total}}]$ at pH 5 and 6.5 generally decreases with increasing aging time. Comparing coprecipitates made with the same OC type, the $[C_{\text{total}}]$ at pH 5 is higher than that at pH 6.5 at both the beginning and end of the aging. Comparing coprecipitates made with different OC types but with similar C loadings, Fh_Hex2/6_7.0 wt%C retains less $[C_{\text{total}}]$ compared to Fh_But3/7_6.0 wt%, 7.3 wt% and 7.8 wt% during the aging process.

3.4.2. Temporal changes of non-desorbable C in the solid phase

The changes in the amount of non-desorbable C ($[C_{\text{non-desorbable}}]$) as a function of aging time at pH 5 and 6.5 are shown in Fig. 5 and summarized in Table 2b. For Fh_Pen1/5 and Fh_Hex2/6 the $[C_{\text{non-desorbable}}]$ at pH 5 and 6.5 generally decreases with increasing aging time. For Fh_But3/7 the $[C_{\text{non-desorbable}}]$ at pH 5 and 6.5 is relatively stable over 12 days aging, with a small decrease at 19 days aging. Comparing coprecipitates made with the same OC type, the $[C_{\text{non-desorbable}}]$ at pH 5 is similar to that at pH 6.5. Comparing coprecipitates made with different OC types but with similar C loadings, Fh_Hex2/6_7.0 wt%C retains less $[C_{\text{non-desorbable}}]$ compared to Fh_But3/7_6.0 wt%, 7.3 wt% and 7.8 wt% during the aging process.

Table 1

SSA and TPV for pure Fh, Fh_Pen1/5_1.2 wt%C, Fh_Hex2/6_7.0 wt%C and Fh_But3/7_7.3 wt%C after 19 days aging at pH 6.5.

	SSA for Fe minerals after 19 days aging (m^2/g) ^a	TPV for Fe minerals after 19 days aging (cm^3/g) ^a
Pure Fh	33 ± 0.1	0.11 ± 0.02
Fh_Pen1/5_1.2 wt%C	46 ± 0.1	0.13 ± 0.02
Fh_Hex2/6_7.0 wt%C	64 ± 0.6	0.22 ± 0.04
Fh_But3/7_7.3 wt%C	103 ± 0.9	0.16 ± 0.02

^a Fe minerals were treated with 0.1 M NaOH for 24 h to desorb OC.

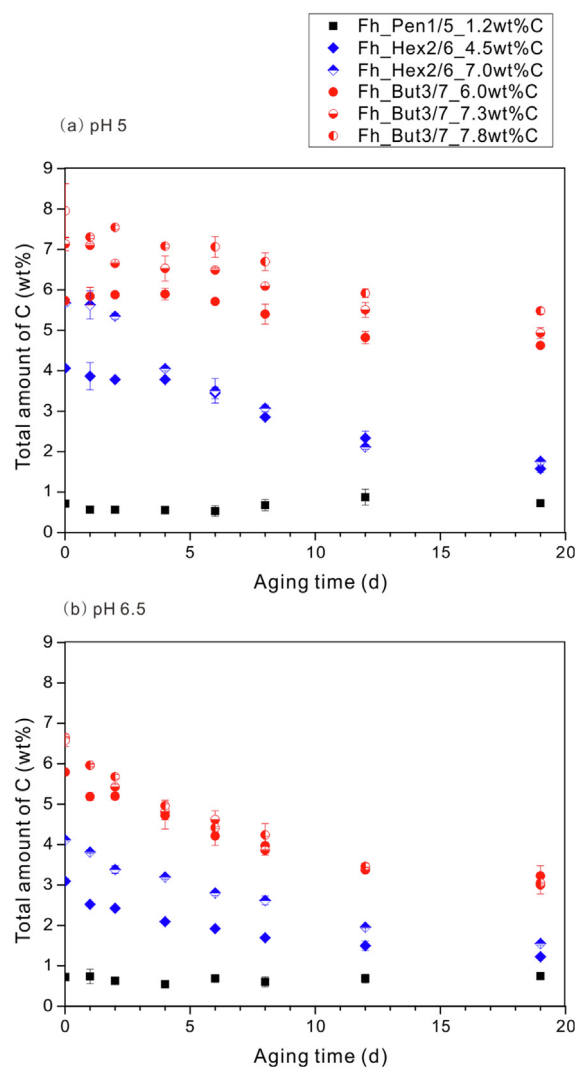


Fig. 4. Temporal changes in the total amount of C in the Fh coprecipitate solid phase during 19 days aging at a) pH 5.0 and b) pH 6.5. Experiments were performed with Fh coprecipitates in 0.01 M NaNO_3 background electrolyte and a solid-solution ratio of 2 g dry sorbent L^{-1} at 75 °C, and sub-samples were collected at 3 h, 1, 2, 4, 6, 8, 12 and 19 days. Black, blue and red symbols represent Pen1/5, Hex2/6 and But3/7 data, respectively. Pen1/5, Hex2/6 and But3/7 represent simple carboxyl-rich OC with one, two and three carboxyl groups, respectively. Error bars represent standard deviations of at least duplicate samples. (For interpretation of the references to colour in this figure legend, the reader is referred to the web version of this article.)

4. Discussion

4.1. Sequestration of carboxyl-rich OC with ferrihydrite prior to aging

4.1.1. Binding strength and distribution of carboxyl-rich OC with ferrihydrite coprecipitates

The reduction in amplitude and shift of the NEXAFS carboxyl peak for our Fh coprecipitates compared to their respective standards (Fig. 1) is consistent with the distortion and/or shift of the FTIR carboxyl bands observed during carboxylic OC adsorption and coprecipitation with Fe (oxyhydr)oxides (Chen et al., 2014; Chorover and Amistadi, 2001; Gu et al., 1994; Kaiser and Guggenberger, 2007; Kaiser et al., 1997; Zeng et al., 2020) and with the distortion (Chen et al., 2014) and both the distortion and shift (Curti et al., 2021) of the NEXAFS carboxyl peak during adsorption and coprecipitation with Fh, and indicates carboxylate-Fe bond formation via a ligand exchange mechanism (Chen et al., 2014;

Table 2a
Total amount of C in the Fh coprecipitates before and after 19 days aging.

Fh coprecipitates	total amount of C (wt%C) at pH 5.00		total amount of C (wt%C) at pH 6.5	
	Before aging	After aging	Before aging	After aging
Fh_Pen1/5_1.2 wt%C	0.72 ± 0.00	0.72 ± 0.03	0.72 ± 0.08	0.75 ± 0.02
Fh_Hex2/6_4.5 wt%C	4.06 ± 0.06	1.58 ± 0.09	3.09 ± 0.06	1.23 ± 0.05
Fh_Hex2/6_7.0 wt%C	5.67 ± 0.06	1.76 ± 0.01	4.12 ± 0.02	1.55 ± 0.04
Fh_But3/7_6.0 wt%C	5.73 ± 0.06	4.62 ± 0.03	5.79 ± 0.01	3.23 ± 0.25
Fh_But3/7_7.3 wt%C	7.14 ± 0.17	4.93 ± 0.13	6.65 ± 0.02	3.00 ± 0.22
Fh_But3/7_7.8 wt%C	7.96 ± 0.67	5.48 ± 0.08	6.58 ± 0.15	3.05 ± 0.02

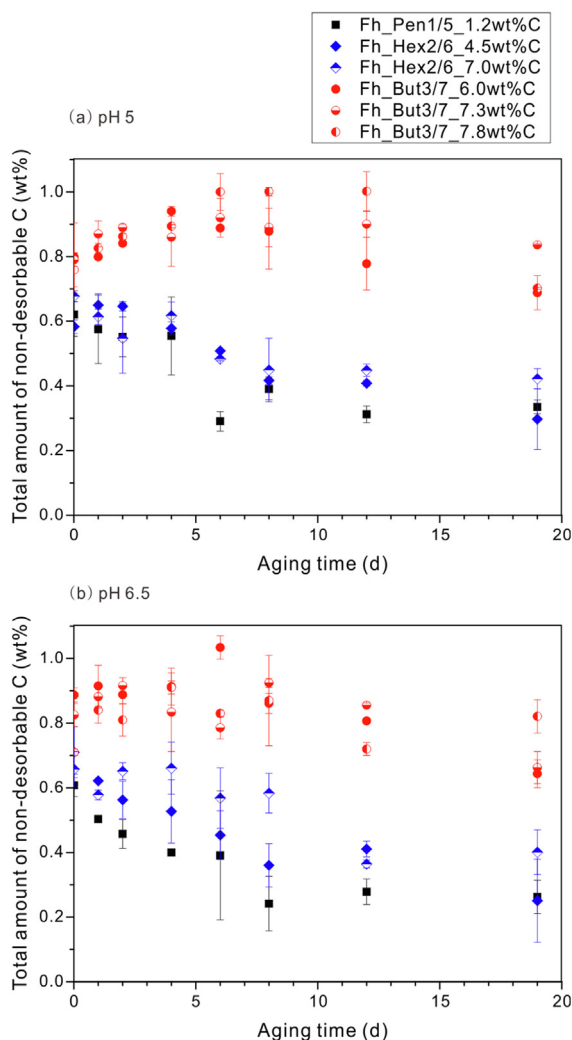


Fig. 5. Temporal changes in the total amount of non-desorbable C in the Fh coprecipitates solid phase during 19 days aging at a) pH 5.0 and b) pH 6.5. Experiments were performed with Fh coprecipitates in 0.01 M NaNO₃ background electrolyte and a solid-solution ratio of 2 g dry sorbent L⁻¹ at 75 °C, and subsamples were collected at 3 h, 1, 2, 4, 6, 8, 12 and 19 days. Black, blue and red symbols represent Pen1/5, Hex2/6 and But3/7 data, respectively. The solid minerals were treated with 0.1 M NaOH for 24 h to extract OC. Pen1/5, Hex2/6 and But3/7 represent simple carboxyl-rich OC with one, two and three carboxyl groups, respectively. Error bars represent standard deviations of at least duplicate samples. (For interpretation of the references to colour in this figure legend, the reader is referred to the web version of this article.)

Chorover and Amistadi, 2001; Curti et al., 2021; Gu et al., 1994; Kaiser and Guggenberger, 2007; Kaiser et al., 1997; Zeng et al., 2020). A shift of the FTIR carboxyl band or NEXAFS carboxyl peak to lower energy compared to the respective standards and an increasing magnitude of this shift, is observed in Fh coprecipitate

systems with constant carboxyl-richness but decreasing OC sequestered (using FTIR, Chen et al., 2014), and in Fh coprecipitate systems with increasing carboxyl-richness and varying OC sequestered (using NEXAFS, Curti et al., 2021). In the former case the shift is attributed to an increasing fraction of the carboxyl groups in each sequestered molecule becoming involved in binding reactions, with decreasing OC sequestered (Chen et al., 2014). In the latter case, and thus in our work here, although the shift is likewise attributed to an increasing number of carboxyl groups per sequestered molecule involved in binding reactions, this increased binding density is independent of the amount of OC sequestered and is rather a function of the richness of structural carboxyl groups within the OC (Curti et al., 2021). As expected, our NEXAFS therefore indicate that the average number of carboxylate-Fe bonds between our carboxyl-rich OC and Fh during coprecipitation increases with increasing carboxyl-richness of the sequestered OC, and thus that the average binding strength of our carboxyl-rich OC increases in the order Pen1/5 < Hex2/6 < But3/7.

During coprecipitation of OC with Fh, OC can be sequestered via adsorption at particle surfaces and also incorporation into mineral particle interiors, for example by being occluded into mineral pore spaces (Eusterhues et al., 2011). In reality there is likely to be a continuum between OC that is adsorbed and OC that is incorporated, in which particle surfaces become saturated and multilayers of OC, macromolecular OC-Fe complexes and OC-Fe (oxyhydr)oxide nanoparticles form with OC occluded into the openings of and inside pores and aggregates (Chen et al., 2014; Lalonde et al., 2012; Lu et al., 2019; Wagai and Mayer, 2007). Our representative STXM image shows that whilst C and Fe are highly spatially correlated, it is difficult to discern whether the C is sequestered via adsorption at particle surfaces and/or incorporation into mineral particle interiors, because the particles are aggregated (Fig. S4). As such the apparent concentration of C around the aggregate rim likely reflects C adsorbed at individual particle surfaces, at the edges of the aggregate where the aggregate is likely thinnest and hence the C signal is strongest, whilst the generally lower apparent concentration of C across the rest of the aggregate likely reflects C adsorbed at individual particle surfaces, inside the bulk of the aggregate where the aggregate is thickest and hence the C signal is weakest (Curti et al., 2021). The generally lower apparent concentration of C across the rest of the aggregate suggests a lack of substantial incorporation of C into individual particle interiors, because the elevated C concentration in the bulk of the aggregate resulting from such incorporation would be expected to mitigate against the aggregate thickness and result in a stronger C signal (see Supplementary Information for further discussion).

In addition to our STXM images, to provide a first order evaluation of the distribution of OC between particle surfaces and interiors, we estimate the surface coverage of our Fh coprecipitates nominally assuming all OC is adsorbed at particle surfaces in a monolayer, without multilayer OC-OC interactions at particle surfaces or incorporation into particle interiors (Table 3). We assume OC is adsorbed via either one (for Pen1/5, Hex2/6 and But3/7), two (for Hex2/6 and But3/7) or three carboxyl groups (for But3/7) per

Table 2b

Total amount of non-desorbable C in the Fh coprecipitates before and after 19 days aging.

Fh coprecipitates	amount of non-desorbable C (wt%C) at pH 5.00		amount of non-desorbable C (wt%C) at pH 6.5	
	Before aging	After aging	Before aging	After aging
Fh_Pen1/5_1.2 wt%C	0.62 ± 0.07	0.34 ± 0.02	0.61 ± 0.03	0.26 ± 0.05
Fh_Hex2/6_4.5 wt%C	0.58 ± 0.02	0.30 ± 0.09	0.71 ± 0.08	0.25 ± 0.13
Fh_Hex2/6_7.0 wt%C	0.68 ± 0.02	0.42 ± 0.03	0.66 ± 0.05	0.40 ± 0.07
Fh_But3/7_6.0 wt%C	0.80 ± 0.10	0.69 ± 0.05	0.89 ± 0.02	0.64 ± 0.04
Fh_But3/7_7.3 wt%C	0.79 ± 0.02	0.84 ± 0.00	0.83 ± 0.04	0.66 ± 0.05
Fh_But3/7_7.8 wt%C	0.76 ± 0.05	0.70 ± 0.00	0.71 ± 0.01	0.82 ± 0.05

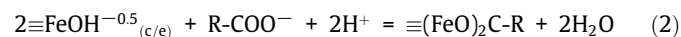
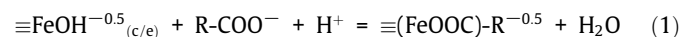
adsorbing molecule and that these adsorption complexes can form between OC and every FeOH site (i.e., there is no steric hindrance). We also adopt the SSA of pure Fh with an uncertainty of ±10% as representative of the SSA of Fh coprecipitated in the presence of OC (Eusterhues et al., 2008; Curti et al., 2021).

Our estimations show that for our Fh_Pen1/5 (6.82 ± 0.68%) and Fh_Hex2/6 coprecipitates (between 22.98 ± 2.30% at the lowest C loading adopting entirely one-carboxyl adsorption and 75.72 ± 7.57% at the highest C loading adopting entirely two-carboxyl adsorption) the amount of OC is significantly less than 100% surface coverage (Table 3). As such this OC could theoretically be adsorbed at Fh particle surfaces in a monolayer, without the need to invoke any extra sequestration capacity that might be provided by adsorption in multilayers and/or incorporation into particle interiors. For our Fh_But3/7 coprecipitates (between 27.62 ± 2.76% at the lowest C loading adopting entirely one-carboxyl adsorption and 113.01 ± 11.30% at the highest C loading adopting entirely three-carboxyl adsorption) the amount of OC is less than or approximately equal to 100% surface coverage (Table 3). As such the majority of this OC could theoretically be adsorbed at Fh particle surfaces in a monolayer, but a minor amount might need to be adsorbed in multilayers at particle surfaces and/or incorporated into particle interiors to account for the total C loading. Previous work on the coprecipitation of Pen1/5, Hex2/6 and But3/7 with Fh (Curti et al., 2021) and the coprecipitation of natural organic matter (NOM) with Fh also indicates that at C:Fe molar ratios below ~1, such as those in this study, most OC is adsorbed at the particle surfaces in a monolayer (or patchy ‘monolayer equivalent’ (Mayer, 1999)), without substantial adsorption in multilayers and/or incorporation into particle interiors (Chen et al., 2014; Curti et al., 2021; Eusterhues et al., 2005; Eusterhues et al., 2008). Taken together our representative STXM image and theoretical estimations indicate that OC in our Fh coprecipitates prior to aging is dis-

tributed as an adsorbed monolayer (or ‘monolayer equivalent’) at particle surfaces.

4.1.2. Binding affinity of carboxyl-rich OC with ferrihydrite

Based on our STXM NEXAFS indicating that our OC is sequestered to Fh coprecipitates via carboxylate-Fe bonds and that these are adsorbed at the particle surfaces, we can quantify the binding affinity of these complexes by conducting adsorption experiments and fitting these to a thermodynamic surface complexation model. Based on our STXM NEXAFS for Pen1/5 we invoke the formation of carboxylate-Fe complexes that adsorb via one-carboxyl adsorption (Fig. 6a) in either a single-bonded (to one FeOH site) (reaction (1)) or twice-bonded (to two FeOH sites) (reaction (2)) configuration. One-carboxyl adsorption is consistent with previous NEXAFS for adsorption of Pen1/5 to Fh (Curti et al., 2021) and attenuated total reflectance (ATR) spectroscopy for adsorption of other monocarboxylic acids to metal oxides (Dobson and McQuillan, 1999):



Based on our STXM NEXAFS for Hex2/6 we invoke the formation of carboxyl ligand exchange complexes that adsorb via two-carboxyl adsorption (Fig. 6b), using two FeOH sites in a bidentate mononuclear or bidentate binuclear configuration, respectively (Curti et al., 2021) (both represented by reaction (3)). Two-carboxyl adsorption is consistent with previous NEXAFS for adsorption of Hex2/6 and other di-carboxylic acids to Fh (Curti et al., 2021) and previous ATR spectroscopy for adsorption of Hex2/6 and other di-carboxylic acids to metal oxides (Dobson and McQuillan, 1999). Previous ATR spectroscopy for Hex2/6 adsorption to Hm (Duckworth and Martin, 2001) however, sug-

Table 3

Surface coverage of Fh coprecipitates by adsorbed C.

Fh coprecipitates	Dry weight (g)		SSA (m ² /g) ^a		Site density (sites/nm ²) ^b		Number of surface sites (mmol sites)	
	Organic wt%	Mineral wt%	Total surface sites of Fh (mmol) ^c	Total amount of C (mmol)	Coverage of Fh with one carboxyl adsorbed (%)	Coverage of Fh with two carboxyl adsorbed (%)	Coverage of Fh with three carboxyl adsorbed (%)	
Pure ferrihydrite	0.10		300					
$\equiv\text{FeOH}^{-0.5(e)}$ sites					2.5		0.125	
$\equiv\text{FeOH}^{-0.5(c)}$ sites					3.7		0.174	
Total amount							0.299	
Fh coprecipitates	Organic wt%	Mineral wt%	Total surface sites of Fh (mmol) ^c	Total amount of C (mmol)	Coverage of Fh with one carboxyl adsorbed (%)	Coverage of Fh with two carboxyl adsorbed (%)	Coverage of Fh with three carboxyl adsorbed (%)	
Fh_Pen1/5_1.2wt%C	2.04	97.96	0.2929 ± 0.0293	0.0200	6.82 ± 0.68			
Fh_Hex2/6_4.5wt%C	9.12	90.88	0.2717 ± 0.0272	0.0624	22.98 ± 2.30	45.96 ± 4.60		
Fh_Hex2/6_7.0wt%C	14.18	85.82	0.2566 ± 0.0257	0.0971	37.86 ± 3.79	75.72 ± 7.57		
Fh_But3/7_6.0wt%C	13.58	86.44	0.2585 ± 0.0259	0.0714	27.62 ± 2.76	55.23 ± 5.52	82.84 ± 8.28	
Fh_But3/7_7.3wt%C	16.50	83.50	0.2497 ± 0.0250	0.0868	34.76 ± 3.47	69.56 ± 6.96	104.34 ± 10.43	
Fh_But3/7_7.8wt%C	17.63	82.37	0.2463 ± 0.0246	0.0928	37.68 ± 3.77	75.34 ± 7.53	113.01 ± 11.3	

^a SSA of pure Fh measured after synthesis.

^b fixed at those calculated by Moon and Peacock (2013).

^c estimated using the surface site density of pure ferrihydrite and the weight mass ratio of the mineral end-member in each coprecipitate; an uncertainty of ±10% on the SSA of pure Fh is assumed in order to take account of the differences in SSA of pure Fh compared to Fh coprecipitates (Eusterhues et al., 2008).

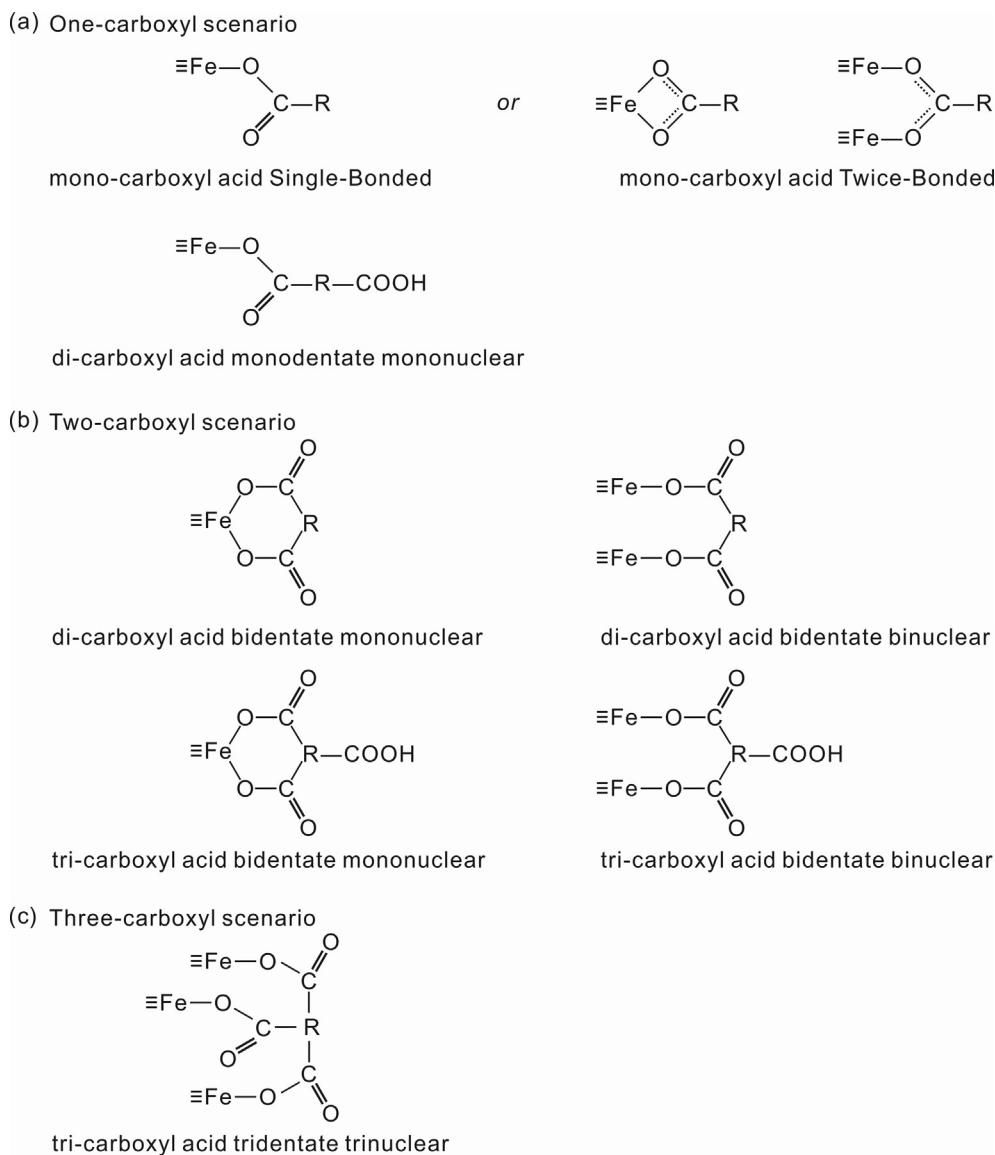
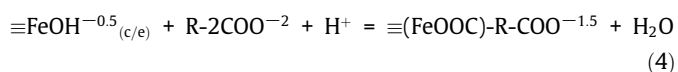
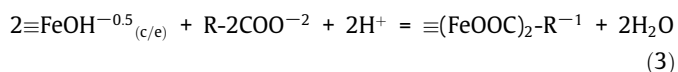


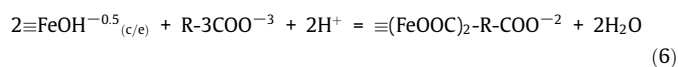
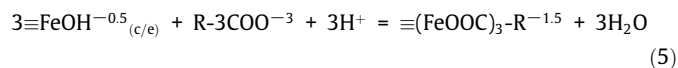
Fig. 6. Possible adsorption configurations of carboxylic acids adsorbed to Fe (oxyhydr)oxides from spectroscopic evidence: a) One-carboxyl adsorption in which mono-carboxylic acids adsorb via their one carboxyl group in either a single-bonded or twice-bonded configuration, and di-carboxylic acids adsorb via one carboxyl group which binds to one FeOH site in a monodentate mononuclear configuration; b) Two-carboxyl adsorption in which di- and tri-carboxylic acids adsorb using two carboxyl groups which bind to either one FeOH site in a bidentate mononuclear configuration or two FeOH sites in a bidentate binuclear configuration; and c) Three-carboxyl adsorption in which tri-carboxylic acids adsorb using three carboxyl groups in a tridentate trinuclear configuration.

gests that Hex2/6 might adsorb to Fe (oxyhydr)oxides via one-carboxyl adsorption using one FeOH site in a monodentate mononuclear configuration (Fig. 6a), possibly because of the steric constraint on the formation of a bidentate structure (reaction (4)):



Based on our STXM NEXAFS for But3/7 we invoke the formation of carboxyl ligand exchange complexes that adsorb via three-carboxyl adsorption, in a tridentate trinuclear configuration (Fig. 6c) (reaction (5)). Three-carboxyl adsorption is consistent with previous NEXAFS work for adsorption of But3/7, propanetricarboxylic and ethanetricarboxylic acid to Fh (Curti et al., 2021) and infrared spectroscopy for adsorption of other tricarboxylic

acids to Fh and Gt (Cornell and Schindler, 1980). Previous FTIR spectroscopy for propanetricarboxylic acid adsorption to Gt (Lindgren et al., 2009) however, suggests that But3/7 might adsorb to Fe (oxyhydr)oxides via two-carboxyl adsorption, possibly in a bidentate mononuclear chelate configuration (Fig. 6b) (reaction (6)), which also represents a bidentate binuclear configuration):



Our STXM NEXAFS results and our model are consistent with a carboxylate-Fe ligand exchange mechanism to explain the bonding environment and distribution of OC. Previous spectroscopic work on the sequestration of carboxylic acids and carboxylic-rich OC

to Fe (oxyhydr)oxides invokes both a direct and indirect coordination between carboxyl groups and Fe ions, in which directly coordinated complexes can be favoured at low pH and indirectly coordinated complexes can be favoured at basic pH (Han et al., 2020). Dampening, broadening and shifts in a spectroscopically identified carboxyl peak as observed in our NEXAFS results, are typically the result of direct coordination between carboxyl groups and Fe ions, which causes significant intramolecular changes and thus alters the absorbance signature of the carboxyl peak (Boily et al., 2000). Since these features are common to all our spectra, we attribute our OC sequestration most likely to direct coordination between carboxyl groups and Fe ions. Dominant formation of indirectly coordinated complexes is expected to cause only minor or unresolvable changes to the peak features (Boily et al., 2000).

For Pen1/5, Hex2/6 and But3/7 we fit each possible surface complexation reaction to the adsorption data individually and in combination with other possible reactions for that carboxylic acid, and consider each reaction with protonated and deprotonated non-bonded carboxyl group(s). The best fitting combination of surface complexation reactions for each carboxylic acid is listed in Table 4 and shown on the adsorption data in Fig. 7.

For Pen1/5 the model fits suggest one-carboxyl adsorption occurring on both FeOH edge and corner sites (Fig. 7a) in a single-bonded monodentate configuration (reaction (1); Fig. 6a) with a binding constant of Log K 9.2 (Table 4). For Hex2/6 the model fits suggest a combination of both two-carboxyl and one-carboxyl adsorption occurring on both FeOH edge and corner sites (Fig. 7b). The two-carboxyl adsorption occurs in a bidentate mononuclear or bidentate binuclear configuration (reaction (3); Fig. 6b) with a binding constant of Log K 16.8 (Table 4). The one-carboxyl adsorption occurs in a monodentate mononuclear configuration (reaction (4); Fig. 6a), in which the non-bonding carboxyl group is protonated at low pH (<pH ~ 5.0) with a binding constant

of Log K 10.5 (Table 4) and deprotonated at higher pH (>pH ~ 5.0) with a binding constant of Log K 15.4 (Table 4). Finally for But3/7 the model fits suggest a combination of both three-carboxyl and two-carboxyl adsorption occurring on both FeOH edge and corner sites (Fig. 7c). The three-carboxyl adsorption occurs in a tridentate trinuclear configuration (reaction (5), Fig. 6c) with a binding constant of Log K 26.3 (Table 4). The two-carboxyl adsorption occurs in a bidentate mononuclear or bidentate binuclear configuration (reaction (6); Fig. 6b), in which the non-bonding carboxyl group is protonated at low pH (<pH ~ 4.5) with a binding constant of Log K 19.0 (Table 4) and deprotonated at higher pH (>pH ~ 4.5) with a binding constant of Log K 23.3 (Table 4). The best fit for But3/7 acid is achieved with adjustment of the surface charge distribution to take into account its larger molecular weight and more diffuse charge distribution. Differences in the binding constants for complexes in which the non-bonded carboxyl group is either deprotonated or protonated (one-carboxyl adsorption for Hex2/6 Log K 10.5/15.4 and two-carboxyl adsorption for But3/7 Log K 19.0/23.3) arise because the complexation reaction for the protonated complex (reaction 4b for Hex2/6 and reaction 6b for But3/7, Table 4) combines the complexation reaction (one or two carboxyls reacting with FeOH) with the protonation reaction of the non-bonded carboxyl group.

Our modelling thus predicts an overall increase in the average number of bonds per sequestered acid molecule and an overall increase in the binding affinity of the sequestered acid molecules in the order Pen1/5 < Hex2/6 < But3/7. The increasing binding affinity of our carboxylic acids explains the macroscopic adsorption behaviour of these acids with Fh, in which adsorption affinity increases in the order Pen1/5 < Hex2/6 ~ But3/7 (Fig. 2). Overall our STXM NEXAFS and model fitting results indicate that the average number of bonds per sequestered acid molecule and thus the binding strength of carboxylic acids to Fe (oxyhydr)oxides increases with increasing carboxyl-richness (Curti et al., 2021).

Table 4
Input parameters for the surface complexation model for adsorption of carboxylic acids on pure Fh.

	Pure Fh			
Specific surface area (m ² /g)	300 ^a			
Site density ≡FeOH _(c) ^{-0.5} (mol sites/g × 10 ⁻³)	1.25 ^b			
Site density ≡FeOH _(e) ^{-0.5} (mol sites/g × 10 ⁻³)	1.74 ^b			
Site density ≡Fe ₃ O ^{-0.5} (mol sites/g × 10 ⁻³)	0.598 ^b			
C _{stern} (F/m ²)	1.10 ^b			
Log K _{FeOH(c)}	≡FeOH _(c) ^{-0.5} + H ⁺ = ≡FeOH _(c) ^{0.5}	7.99 ^b		
Log K _{FeOH(c)_Na}	≡FeOH _(c) ^{-0.5} + Na ⁺ = ≡FeOH _(c) ^{-0.5} -Na ⁺	-1.00 ^b		
Log K _{FeOH2(c)_NO3}	≡FeOH _(c) ^{-0.5} + NO ₃ ⁻ = ≡FeOH _(c) ^{-0.5} -NO ₃ ⁻	-1.00 ^b		
(where equations above are repeated for (≡FeOH _(e) ^{-0.5}))				
Log K _{Fe3O}	≡Fe ₃ O ^{-0.5} + H ⁺ = ≡Fe ₃ OH ^{+0.5}	7.99 ^b		
Log K _{Fe3O_Na}	≡Fe ₃ O ^{-0.5} + Na ⁺ = ≡Fe ₃ O ^{-0.5} -Na ⁺	-1.00 ^b		
Log K _{Fe3OH_NO3}	≡Fe ₃ OH ^{+0.5} + NO ₃ ⁻ = ≡Fe ₃ OH ^{+0.5} -NO ₃ ⁻	-1.00 ^b		
			pKa ₁	pKa ₂
Pentanoic acid (Pen1/5)			4.84 ^c	
Hexanedioic acid (Hex2/6)			4.42 ^c	5.41 ^c
Butane 1, 2, 4 tricarboxylic acid (But3/7)			4.31 ^d	4.82 ^d
				5.21 ^d
		Δz ₀	Δz ₁	
			Pen1/5	Hex2/6
				But3/7
1. Log K _{FeOH(c/e)_OOC-R}	≡FeOH _(c/e) ^{-0.5} + R-COO ⁻ + H ⁺ = ≡(FeOOC)-R ^{-0.5} + H ₂ O	+0.5 ^e	-0.5 ^e	9.2 ^e
3. Log K _{FeOH(c/e)_OOC-R}	2≡FeOH _(c/e) ^{-0.5} + R-2COO ⁻² + 2H ⁺ = ≡(FeOOC) ₂ -R ⁻¹ + 2H ₂ O	+1.0 ^e	-1.0 ^e	16.8 ^e
4a. Log K _{FeOH(c/e)_OOC-R}	≡FeOH _(c/e) ^{-0.5} + R-2COO ⁻² + H ⁺ = ≡(FeOOC)-R-COO ^{-1.5} + H ₂ O	+0.5 ^e	-0.5 ^e	10.5 ^e
4b. Log K _{FeOH(c/e)_OOC-R}	≡FeOH _(c/e) ^{-0.5} + R-2COO ⁻² + 2H ⁺ = ≡(FeOOC)-R-COOH ^{-0.5} + 2H ₂ O	+0.5 ^e	-0.5 ^e	15.4 ^e
5. Log K _{FeOH(c/e)_OOC-R}	3≡FeOH _(c/e) ^{-0.5} + R-3COO ⁻³ + 3H ⁺ = ≡(FeOOC) ₃ -R ^{-1.5} + 3H ₂ O	+1.3 ^e	-0.3 ^e	26.3 ^e
6a. Log K _{FeOH(c/e)_OOC-R}	2≡FeOH _(c/e) ^{-0.5} + R-3COO ⁻³ + 2H ⁺ = ≡(FeOOC) ₂ -R-COO ⁻² + 2H ₂ O	+1.3 ^e	-0.3 ^e	19.0 ^e
6b. Log K _{FeOH(c/e)_OOC-R}	2≡FeOH _(c/e) ^{-0.5} + R-3COO ⁻³ + 3H ⁺ = ≡(FeOOC) ₂ -R-COOH ⁻¹ + 2H ₂ O	+1.95 ^e	-0.45 ^e	23.3 ^e

^a measured in this study;

^b from Moon and Peacock (2013);

^c from Dean (1987);

^d calculated using ACD/I-Lab 2.0 (ACD/I-Lab, version 2.0, Advanced Chemistry Development, Inc);

^e fit in this study.

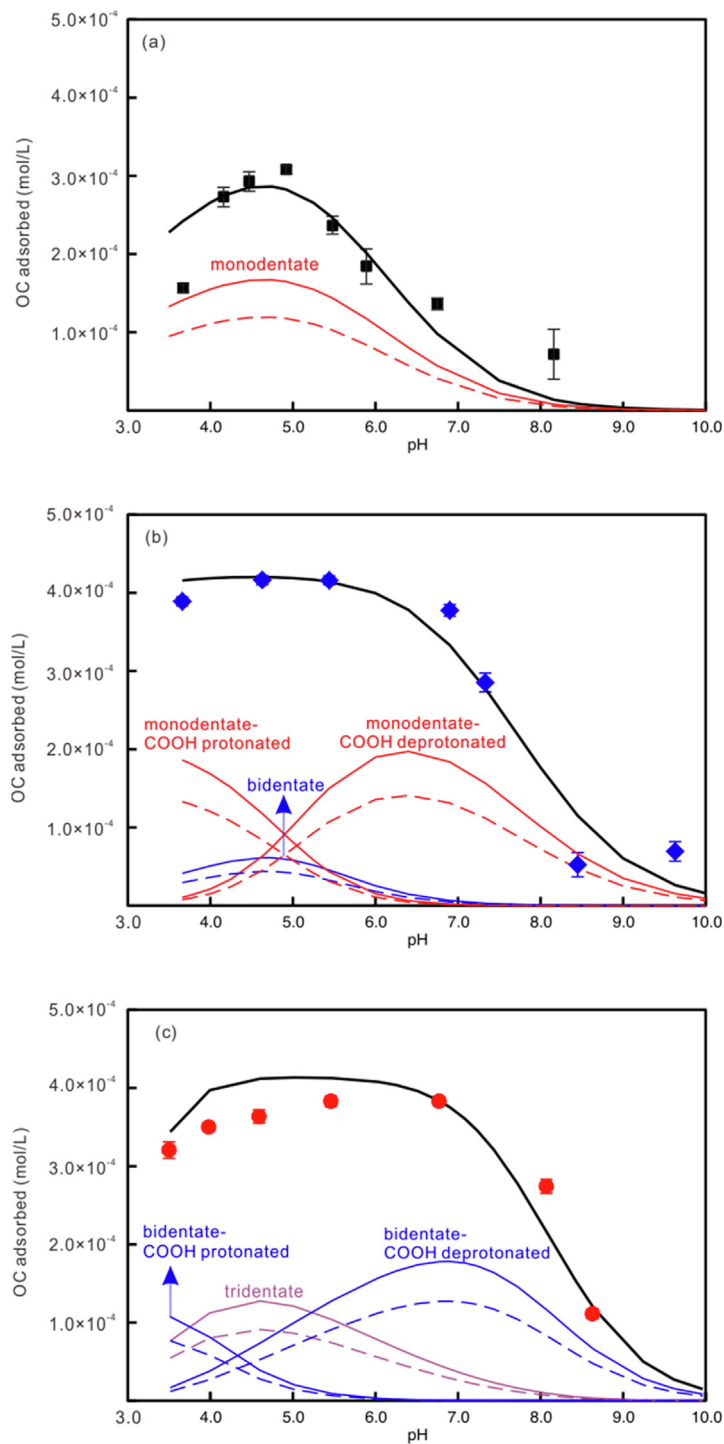


Fig. 7. Surface species for: a) Pen1/5, b) Hex2/6 and c) But3/7 as function of pH based on complexation model fits (lines) to adsorption data (symbols). Black, blue and red symbols represent Pen1/5, Hex2/6 and But3/7 data, respectively. Monodentate (red lines), bidentate (blue lines) and tridentate (purple lines) represent one, two and three carboxyl binding, respectively, via corner sharing complexation (solid red, blue, purple lines) and edge-sharing complexation (dashed red, blue, purple lines). The black solid lines are the sum of the modelled species, representing the total amount of OC adsorbed. Pen1/5, Hex2/6 and But3/7 represent simple carboxyl-rich OC with one, two and three carboxyl groups, respectively. Error bars represent standard deviations of at least duplicate samples. (For interpretation of the references to colour in this figure legend, the reader is referred to the web version of this article.)

4.2. Influence of carboxyl-rich OC on the aging of ferrihydrite

4.2.1. Kinetics of Fh aging influenced by carboxyl-rich OC

Our experiments show that the presence of OC retards the aging of Fh to more crystalline Fe minerals (Fig. 3a and 3b), which is consistent with previous reports that additives of carboxylic acids,

humic acids and other kinds of OC can retard the aging of Fh to crystalline iron minerals (Cornell and Schwertmann, 1979; Cornell, 1985; Hu et al., 2018; Lu et al., 2019). In oxic environments aging of Fh to more crystalline iron minerals occurs via dissolution-recrystallisation or solid-state aggregation: aggregation of Fh followed by nucleation and crystal growth within the aggregate

(Cornell and Schwertmann, 1979; Cudennec and Lecerf, 2006; Schwertmann and Fischer, 1966). The presence of OC can influence the factors that control dissolution–recrystallisation and/or solid-state aggregation and thus can affect aging rate, for example, OC can block surface sites and subsequently prevent the dissolution of iron (oxyhydr)oxide to form goethite or the nucleation of hematite (Kaiser and Guggenberger, 2003); OC can complex with aqueous Fe(III) to inhibit nucleation (Cornell and Schwertmann, 1979); and OC can influence Fh aggregation and associate with the surface of neofomed mineral nuclei and crystals to inhibit crystal growth (Amstaetter et al., 2012; Eusterhues et al., 2008).

For the aging of our Fh coprecipitates compared to pure Fh, it is clear that the retardation effect of OC generally increases in the order Pen1/5 < Hex2/6 < But3/7 (at pH 5) and Pen1/5 < Hex2/6 ~ But3/7 (at pH 6.5) and thus with increasing carboxylic acid binding strength (Fig. 3a and 3b). Previous work reports the influence of aqueous (hydroxyl)-carboxylic acids on the aging of Fh to other more crystalline Fe minerals, where the retardation of aging is also related to the relative adsorption affinity of the acids to Fh (Cornell and Schwertmann, 1979). For Fh coprecipitates made with different OC types but with similar C loadings, our surface complexation modelling indicates that the number of bonds formed between the OC and Fh particles is equal to the number of –FeOH sites used, and both the number of bonds formed and the sites used increase with the carboxyl-richness, where the former controls the binding strength (Fridde et al., 2012) and the latter influences the surface coverage. Therefore both the binding strength and surface coverage for a similar adsorbed amount of our different carboxylic acids follow the order Pen1/5 < Hex2/6 < But3/7. As such there is greater blocking of Fh surface sites and thus a greater retardation of dissolution and recrystallisation in the order Pen1/5 < Hex2/6 < But3/7 (Kaiser and Guggenberger, 2003).

It is also clear that the retardation effect of OC is related to increasing C loading and pH. In general as C loading increases at pH 5 the retardation of aging increases from Fh-Pen1/5_1.2 wt%C to Fh_But3/7_7.8 wt%C, but individual coprecipitates Fh_Hex2/6_2.9 wt%C, Fh_Hex2/6_4.1 wt%C and Fh_But3/7_6.0 wt%C show similar behaviour (Fig. 3a). As C loading increases at pH 6.5 however, the retardation of aging increases from Fh-Pen1/5_1.2 wt%C to Fh_But3/7_7.8 wt%C, but individual Fh_Hex2/6 and Fh_But3/7 coprecipitates all show similar behaviour (Fig. 3b). Furthermore at pH 6.5, whilst the retardation of aging for the Fh_Pen1/5 and Fh_Hex2/6 coprecipitates is similar to that at pH 5, the retardation of aging for the Fh_But3/7 coprecipitates is reduced (comparing Fig. 5a and 5b). The effect of C loading on retardation of aging may be explained by considering the fact that, because our acids are mostly adsorbed at particle surfaces (Curti et al., 2021), increased C loading results in higher surface coverage and thus a greater retardation of dissolution and recrystallisation (Kaiser and Guggenberger, 2003). Increased C loading can also lead to greater retardation of aging through the complexation of OC with aqueous Fe(III) to inhibit nucleation (Cornell and Schwertmann, 1979) and the association of OC with the surface of newly formed mineral nuclei and crystals to inhibit crystal growth (Amstaetter et al., 2012; Eusterhues et al., 2008). For individual coprecipitates Fh_Hex2/6_2.9 wt%C and Fh_Hex2/6_4.1 wt% C, made with the same OC type but increasing C loading, it appears that the C loading effect cannot indefinitely increase retardation. We suppose that there is a maximum retardation effect for simple carboxyl-rich OC, but this requires further investigation.

The effect of pH on OC retardation of aging may be explained by the fact that under acidic conditions (pH < 7) Fh ages via dissolution–recrystallisation, whereas under neutral conditions (pH ~ 7) Fh ages mainly via solid-state aggregation: aggregation of Fh followed by nucleation and crystal growth within the aggre-

gate (Cornell and Schwertmann, 1979; Cudennec and Lecerf, 2006; Schwertmann and Fischer, 1966). During dissolution–recrystallisation processes, OC can block surface sites to directly retard the aging process, but during solid-state aggregation this retardation mechanism may be less effective and instead OC might associate with mineral nuclei and newly formed crystals to inhibit oriented aggregation of pure mineral clusters and crystal growth of more crystalline minerals (Amstaetter et al., 2012; Eusterhues et al., 2008). In addition OC may act as a bridging molecule between mineral particles and then stabilise them as low-density aggregates (Amstaetter et al., 2012; Illés and Tombácz, 2006). These more indirect mechanisms for retardation of aging may account for the similarity in the retardation of individual Fh_Hex2/6 and Fh_But3/7 coprecipitates, and the reduction in retardation of Fh_But3/7 coprecipitates at pH 6.5 compared to pH 5. Furthermore, whilst adsorption of negatively charged OC onto positively charged Fe minerals creates negatively charged OC-coated particles that repel one another and hinder aggregation (Illés and Tombácz, 2006), recent work shows that OC with MW < 3 kDa is unable to completely stabilise mineral particles via steric repulsion (Li et al., 2020). This may also contribute to the reduction in retardation of Fh_But3/7 coprecipitates at pH 6.5 compared to pH 5, and again suggests that increasing C loading of simple organic molecules may not result in increased retardation of aging, although this requires further investigation.

4.2.2. Properties of Fh coprecipitates after aging influenced by carboxyl-rich OC

Our results show that the SSA of the Fe minerals after aging of pure Fh ($33 \pm 0.1 \text{ m}^2/\text{g}$) are significantly less than the SSA of unaged pure Fh ($300 \text{ m}^2/\text{g}$), and that the Fe minerals after aging of Fh coprecipitates (46 ± 0.1 – $103 \pm 0.9 \text{ m}^2/\text{g}$) are also significantly less than the SSA of un-aged Fh coprecipitates (taken as $300 \text{ m}^2/\text{g}$ with an uncertainty of $\pm 10\%$) (Table 1). In agreement with previous work, it is clear that in both the pure Fh and Fh coprecipitate systems, the Fe minerals present after aging have significantly reduced SSA and thus larger particle size and/or higher crystallinity (Das et al., 2011; Hu et al., 2018), but it is also apparent that the influence of OC in the Fh coprecipitate systems somewhat mitigates against the decline in SSA. This is likely because OC retards the aging of Fh to more crystalline minerals and inhibits mineral crystal growth (Cornell and Schwertmann, 1979; Kaiser and Guggenberger, 2003). Thus compared to pure Fh systems, this results in Fe minerals with smaller particle size and/or lower crystallinity, larger lattice spacings and a more porous surface structure and thus a less compact bulk mineral (Eusterhues et al., 2008), as confirmed by scanning transmission electron microscopy (STEM) observations (Lu et al., 2019).

Our results also show that the SSA and TPV of our Fe minerals after aging of Fh coprecipitates increase with increasing carboxylic acid binding strength (Table 1), and thus follow the order Fh < Fh_Pen1/5_1.2 wt%C < Fh_Hex2/6_7.0 wt%C < Fh_But3/7_7.3 wt%C. In particular, comparing composites with similar C loading but increased binding strength, namely Fh_Hex2/6_7.0 wt%C and Fh_But3/7_7.3 wt%C, the latter has significantly higher SSA. Thus whilst the retardation of aging for Fh_Hex2/6_7.0 wt%C and Fh_But3/7_7.3 wt%C is similar, the more strongly bound But3/7 appears to be able to further inhibit the growth of more crystalline Fe minerals, leading to smaller particle size and/or lower crystallinity and a more porous structure.

4.3. Stability of carboxyl-rich OC during aging of ferrihydrite

4.3.1. Mechanisms for temporal changes in the total amount of C

Our experiments show that the total amount of C with our Fh_Pen1/5_1.2 wt%C coprecipitate is essentially invariant with

aging time at pH 5 and 6.5, whilst the total amount of C with our Fh_Hex2/6 and Fh_But3/7 coprecipitates decreases with aging time at pH 5 and 6.5 (Fig. 4a and 4b). These trends may be understood by considering the binding strength of the OC and the properties of Fe minerals after aging of Fh.

Given the SSA of Fe minerals formed after aging of Fh coprecipitates (Table 1) we can estimate their surface coverage at the end of aging (after 19 days) following the same approach used to estimate the surface coverage of the initial Fh coprecipitates above (section 4.1.1). Our estimations show that the aged Fh_Pen1/5_1.2 wt%C still appears to have sufficient SSA (Table 5) to theoretically accommodate all the initial OC in an adsorbed monolayer at the particle surfaces (surface coverage 37.37%, Table 5a) and a total theoretical adsorption capacity (3.04 wt%C, Table 5b) that is well in excess of both the total initial amount of C (1.2 wt%C) and the total remaining amount of C (0.72–0.75 wt%, Table 5b). This might explain why the total remaining amount of C for Fh_Pen1/5_1.2 wt%C is essentially invariant with aging time (Fig. 4a and 4b), and implies that both the total initial amount of C and the total remaining amount of C could be adsorbed at the particle surfaces.

The aged Fh_Hex2/6_7.0 wt%C appears to have insufficient SSA (Table 5) to theoretically accommodate all the initial OC in an adsorbed monolayer at the particle surfaces (surface coverage between 130.58% adopting entirely monodentate adsorption and 261.15% adopting entirely bidentate adsorption, Table 5a) and a total theoretical adsorption capacity (between 2.54 wt%C adopting entirely bidentate adsorption and 4.84 wt%C adopting entirely monodentate adsorption, Table 5b) that is well below the total initial amount of C (7.0 wt%C) but still in excess of the total remaining amount of C (1.55–1.76 wt%, Table 5b). This might explain why the total remaining amount of C for the Fh_Hex2/6 coprecipitates decreases with aging time (Fig. 4a and 4b), but akin to Fh_Pen1/5_1.2 wt%C, implies that both the total initial amount of C and the total remaining amount of C are adsorbed at the particle surfaces.

In contrast the aged Fh_But3/7_7.3 wt%C appears to have insufficient SSA (Table 5) to theoretically accommodate all the initial OC in an adsorbed monolayer at the particle surfaces (surface coverage between 145.05% adopting entirely bidentate adsorption and 217.57% adopting entirely tridentate adsorption, Table 5a) and a total theoretical adsorption capacity (between 3.12 wt%C adopting entirely tridentate adsorption and 4.52 wt%C adopting entirely bidentate adsorption, Table 5b) that is well below the total initial amount of C (7.3 wt%C) but not in excess of the total remaining amount of C (3.00–4.90 wt%, Table 5b). This might explain why the total remaining amount of C for the Fh_But3/7 coprecipitates decreases with aging time (Fig. 4a and 4b), but unlike Fh_Pen1/5_1.2 wt%C and the Fh_Hex2/6 coprecipitates, implies that, whilst the total initial amount of C is adsorbed at the particle surfaces, some part of the total remaining amount of C might be incorporated into the particle interiors.

These estimations therefore indicate that the amount of OC retained by Fh coprecipitates during the aging process is strongly coupled to the binding strength of the OC molecules and the initial C loading of the coprecipitates. For Fh coprecipitated with rela-

tively carboxyl-poor OC and with low initial C loading such as Fh_Pen1/5_1.2 wt%C, we suggest that net OC release is essentially minimal during aging because the Fe minerals formed after aging have sufficient adsorption capacity to accommodate all the initial OC at the particle surfaces. For Fh coprecipitated with relatively carboxyl-rich OC and with higher but essentially equivalent initial C loading such as Fh_Hex2/6_7.0 wt%C and Fh_But3/7_7.3 wt%C, we suggest that net OC release is significant during aging because the Fe minerals formed after aging have insufficient adsorption capacity to accommodate all the initial OC at the particle surfaces. For these relatively carboxyl-rich coprecipitates we suggest that the remaining OC is partitioned between the mineral surfaces and the particle interiors, and that this partitioning is strongly influenced by the binding strength of the OC because this controls both the initial C loading of the coprecipitates and the physiochemical properties of the Fe minerals after aging.

4.3.2. Mechanisms for temporal changes in non-desorbable C

We can shed further light on the stability of OC during aging as a function of the binding strength of the OC molecules and C loading of the coprecipitates by considering our results for non-desorbable C. In our work we operationally define non-desorbable C as C that cannot be removed from the solid particles with 0.1 M NaOH (Kaiser and Guggenberger, 2007). Previous work on the coprecipitation of Pen1/5, Hex2/6 and But3/7 with Fh using the same experimental coprecipitation conditions as used here (Curti et al., 2021) shows that at C:Fe molar ratios ~0.1–0.8, equivalent to those used in this study, between ~10–30% of OC adsorbed in a monolayer at the Fh particle surfaces remains adsorbed after washing with 0.1 M NaOH and is thus very strongly adsorbed at particle surfaces or is incorporated into particle interiors, for example by being occluded into mineral pore spaces (Kaiser and Guggenberger, 2007; Lu et al., 2019).

Our experiments show that the total amount of non-desorbable C with our Fh_Pen1/5_1.2 wt%C and Fh_Hex2/6 coprecipitates decreases with aging time, while the total amount of non-desorbable C with our Fh_But3/7 coprecipitates is relatively stable over the first 12 days of aging then decreases after 19 days aging time (Fig. 5a and 5b). Given that our surface coverage estimations for the Fh coprecipitates after 19 days aging suggest that the adsorption capacity of the Fe minerals formed after aging of Fh_Pen1/5_1.2 wt%C (3.04 wt%, Table 5b) and Fh_Hex2/6_7.0 wt%C (2.54–4.84 wt%, Table 5b) are well in excess of the total remaining amount of C (0.72–0.75 wt% for Fh_Pen1/5_1.2 wt%, and 1.55–1.76 wt% for Fh_Hex2/6_7.0 wt%, Table 5b), it is therefore possible that both the desorbable and the non-desorbable part of this total remaining C is adsorbed at the particle surfaces. In turn this suggests that the total remaining C after aging is comprised of two pools with differing stabilities; a relatively loosely bound desorbable pool that is released after washing with 0.1 M NaOH and a relatively strongly bound non-desorbable pool that is retained after washing with 0.1 M NaOH. The presence of a loosely bound desorbable pool and more strongly bound non-desorbable pool after repeated washing with 0.1 M NaOH is also observed for unaged Fh_Pen1/5 and Fh_Hex2/6 coprecipitates and attributed to

Table 5a
Surface coverage of Fe minerals for Fh_Pen1/5_1.2 wt%C, Fh_Hex2/6_7.0 wt%C and Fh_But3/7_7.3 wt%C after 19 days aging at pH 6.5.

	Total initial C with Fh (wt%)	SSA of Fe minerals after 19 days aging (m ² /g) ^a	Site density of Fe minerals after 19 days aging (sites/nm ²) ^b	Coverage of Fe minerals after 19 days aging with one carboxyl adsorbed	Coverage of Fe minerals after 19 days aging with two carboxyl adsorbed	Coverage of Fe minerals after 19 days aging with three carboxyl adsorbed
Fh_Pen1/5_1.2 wt%C	1.2 wt%	46	7	37.37		
Fh_Hex2/6_7.0 wt%C	7.0 wt%	64	7	130.58	261.15	
Fh_But3/7_7.3 wt%C	7.3 wt%	103	7		145.05	217.57

Table 5b

Adsorption capacity of Fe minerals for Fh_Pen1/5_1.2 wt%C, Fh_Hex2/6_7.0 wt%C and Fh_But3/7_7.3 wt%C after 19 days aging.

	SSA of Fe minerals after 19 days aging (m ² /g) ^a	Site density of Fe minerals after 19 days aging (sites/nm ²) ^b	Adsorption capacity of Fe minerals after 19 days aging (one carboxyl binding)	Adsorption capacity of Fe minerals after 19 days aging (two carboxyl binding)	Adsorption capacity of Fe minerals after 19 days aging (three carboxyl binding)	Total remaining C with Fe minerals measured after 19 days aging	
						pH 5.0	pH 6.5
Fh_Pen1/5_1.2 wt%C	46	7	3.04 wt%C			0.72 wt %C	0.75 wt %C
Fh_Hex2/6_7.0 wt%C	64	7	4.84 wt%C	2.54 wt%C		1.76 wt %C	1.55 wt %C
Fh_But3/7_7.3 wt%C	103	7		4.52 wt%C	3.12 wt%C	4.90 wt %C	3.00 wt %C

^a SSA of Fe minerals treated with 0.1 M NaOH for 24 h to desorb OC after aging for 19 days at pH 6.5.^b Site density for Fe minerals calculated from average site density of Gt and Hm (Peacock and Sherman, 2004).

the presence of binding strength heterogeneities in the local adsorption environment, such as steric hindrance and/or electrostatic repulsion in a patchy ‘monolayer equivalent’ (Wershaw, 1994), that render some molecules less strongly bound and more susceptible to desorption (Kaiser and Guggenberger, 2007; Curti et al., 2021). In the case of the Hex2/6 acid molecules, these are adsorbed via either a bidentate or monodentate carboxyl adsorption mechanism (Fig. 7b) and as such, those that experience binding strength heterogeneities as above and also those that are monodentate are similarly likely to be more susceptible to desorption (Kaiser and Guggenberger, 2007; Curti et al., 2021).

In contrast given that our surface coverage calculations for the Fh coprecipitates after 19 days aging indicate that the adsorption capacity of Fe minerals after aging of Fh_But3/7_7.3 wt%C (3.12–4.52 wt%C, Table 5b) are not in excess of the total remaining amount of C (3.05–4.90 wt%C, Table 5b), it is therefore likely that some part of the total remaining C is incorporated into the particle interiors where it is more difficult to remove with 0.1 M NaOH (Kaiser and Guggenberger, 2007; Lu et al., 2019). At first glance, the presence of C incorporated into the particle interiors, for example by being occluded into mineral pore spaces (Eusterhues et al., 2011), might be expected to decrease the TPV of aged Fh_But3/7_7.3 wt%C compared to aged pure Fh, however, the TPV results show that the TPV of aged Fh_But3/7_7.3 wt%C (0.16 ± 0.02 cm³/g, Table 1) is somewhat higher than aged pure Fh (0.11 ± 0.02 cm³/g, Table 1) and Fh_Pen1/5_1.2 wt% (0.13 ± 0.02 cm³/g, Table 1). This suggests that the adsorption of desorbable C at shallow pores and pore openings, which is removed by washing with 0.1 M NaOH, creates a more open and porous structure in the aged Fe minerals (Eusterhues et al., 2008), that is then reflected in the higher TPV measurements. In addition, the retardation of aging in the presence of But3/7 results in a small fraction of Fh remaining after 19 days (Fig. 3), which has a more porous structure than the aged Fe minerals, and thus this Fh may also help explain the higher TPV measurements. Overall these results support our suggestion that the partitioning of the remaining OC between the mineral surfaces and the particle interiors after aging depends primarily on the binding strength of the OC because this controls both the initial C loading of the coprecipitates and the physiochemical properties of the Fe minerals after aging.

It is also important to note that the ratio of non-desorbable C to total C changes with the aging process (Fig. 8). For Fh_Pen1/5_1.2 wt%C it is likely that a substantial amount of C is desorbed from the Fh coprecipitates during the washing process, that is necessarily performed after synthesis to remove excess salts. This initial loss of C is relatively large for Fh_Pen1/5_1.2 wt % compared to the Fh_Hex2/6 and Fh_But3/7 coprecipitates, because the Pen1/5 acid molecules are the least strongly adsorbed. At the start of the aging the total C associated with the particles is

thus relatively non-desorbable and the absolute value for the percentage of C that is non-desorbable is ~100% (Fig. 8). It is then clear that during aging, while the total amount of C is relatively constant, the total amount of non-desorbable C decreases, from an amount nearly equivalent to the total amount of C to an amount significantly less than the total amount of C (Figs. 4 and 5). The percentage of total C that is non-desorbable therefore decreases over time from near 100% to ~40% (Fig. 8). This suggests that the fraction of OC that is very strongly adsorbed decreases during aging. For the Fh_Hex2/6 coprecipitates, the total amount of C decreases and the total amount of non-desorbable C decreases but at a lesser rate compared to the total amount of C, and from an amount significantly less than the total amount of C (Figs. 4 and 5). The percentage of total C that is non-desorbable is therefore approximately constant over time at ~15–20% at pH 5 and 20–25% at pH 6 (Fig. 8). This suggests that the fraction of OC that is very strongly adsorbed and/or incorporated is approximately constant during aging. For the Fh_But3/7 coprecipitates, the total amount of C decreases and the total amount of non-desorbable C is relatively constant, but again is significantly less than the total amount of C (Figs. 4 and 5). The percentage of total C that is non-desorbable therefore increases over time from ~10–15% to ~12–25% at pH 5 and 6.5 (Fig. 8). This suggests that the fraction of OC that is very strongly adsorbed and/or incorporated increases during aging.

The overarching trend in the percentage of C that is non-desorbable during aging of the Fh_Pen1/5, Fh_Hex2/6 and Fh_But3/7 coprecipitates, where non-desorbable C for Fh_Pen1/5_1.2 wt%C decreases, for the Fh_Hex2/6 coprecipitates remains relatively constant and for the Fh_But3/7 coprecipitates increases, follows the increasing binding strength of these acid molecules in the order Pen1/5 < Hex2/6 < But3/7. The absolute values for the percentage of C that is non-desorbable before aging for the Fh_Hex2/6 and Fh_But3/7 coprecipitates are also comparable with previous work in which Hex2/6 and But3/7 are coprecipitated with Fh using the same experimental coprecipitation conditions as used here (Curti et al., 2021). In this previous study un-aged Fh_Hex2/6 and Fh_But3/7 coprecipitates with approximately equivalent C:Fe molar ratios to our coprecipitates, have ~15–20% C and ~20–30% C, respectively, that is non-desorbable with 0.1 M NaOH (Curti et al., 2021). Thus for the un-aged Fh_Hex2/6 and Fh_But3/7 coprecipitates we see that a small percentage of the total C is non-desorbable at the start of the aging and that this percentage is approximately constant or increases during the aging as the weakly adsorbed desorbable C is released relative to the strongly adsorbed and/or incorporated non-desorbable C. Our results therefore indicate that relatively carboxyl-rich OC coprecipitated with Fh becomes proportionally more stable with the solid phase and thus less mobile during aging. Our results therefore also indicate that relatively carboxyl-rich OC coprecipitated with Fh is

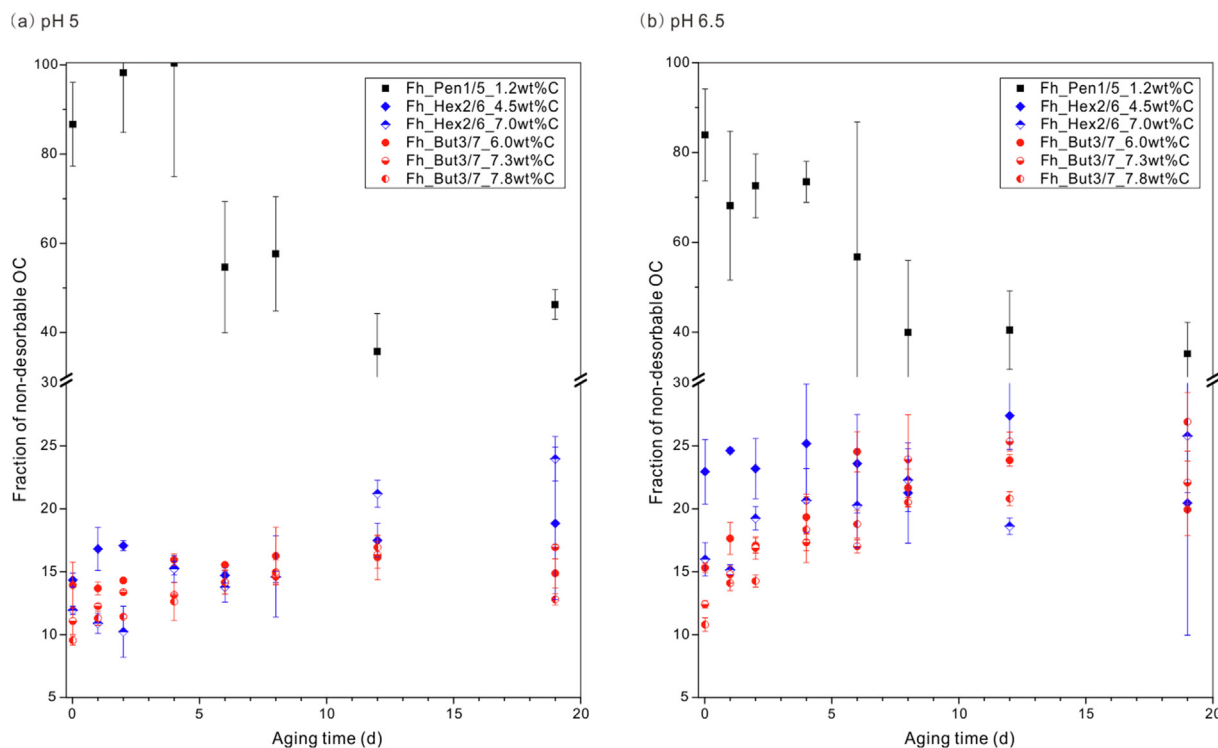


Fig. 8. Percentage of C that is non-desorbable with aging. The percentage of non-desorbable C is calculated by $[C_{\text{non-desorbable}}]/[C_{\text{total}}]$. Black, blue and red symbols represent Pen1/5, Hex2/6 and But3/7 data, respectively. Pen1/5, Hex2/6 and But3/7 represent simple carboxyl-rich OC with one, two and three carboxyl groups, respectively. Error bars represent standard deviations of at least duplicate samples. (For interpretation of the references to colour in this figure legend, the reader is referred to the web version of this article.)

more persistent than relatively carboxyl-poor OC in soils and sediments, which might help to provide a mechanistic explanation for the recently reported relationship between OC-mineral binding strength and OC-mineral persistence over time (Hemingway et al., 2019).

5. Conclusions

Our STXM NEXAFS and adsorption experiment plus surface complexation model results show that the binding strength of our carboxylic acids sequestered to Fh increases with an increasing number of carboxyl functional groups (Pen1/5 < Hex2/6 < But3/7). Regarding the role of OC in the aging of Fh, we show that OC substantially retards the aging of Fe (oxyhydr)oxide to more crystalline Fe minerals and that this retardation increases with increasing binding strength of the OC, following the order Pen1/5 < Hex2/6 < But3/7 at similar C loading, and with increasing C loading and decreasing pH. The SSA and TPV of Fe minerals formed from aging of our Fh coprecipitates also appear to increase with increasing binding strength of the OC, suggesting that OC with higher binding strength is able to further inhibit the growth of more crystalline Fe minerals. Regarding the fate of OC during aging of Fh, we find that the total amount of C retained with the solid during aging is strongly coupled to the binding strength of the OC and the initial C loading of the coprecipitates, where OC with higher binding strength is retained more with the solid by influencing the physicochemical properties of Fe minerals after aging, and partial OC is released if the initial C loading is higher than the adsorption capacity of Fe minerals after aging. We also find that the total amount of non-desorbable C after 19 days aging similarly shows a positive correlation with the binding strength of the OC, where the proportion of non-desorbable C decreases during aging for OC with relatively low binding strength but increases

during aging for OC with relatively high binding strength. Our results suggest that the transition of OC from a relatively low stability pool to a relatively high stability pool during aging is strongly influenced by the binding strength of the OC, because this controls both the initial C loading of the coprecipitates and the physicochemical properties of the Fe minerals after aging. Overall we find that carboxyl-rich OC coprecipitated with Fh becomes proportionally more stable with the solid phase because carboxyl-poor OC that has lower binding strength is more readily released during aging. Our work might therefore offer a deeper mechanistic insight into the mechanisms responsible for the persistence and long-term preservation of OC in natural environments.

Declaration of Competing Interest

The authors declare that they have no known competing financial interests or personal relationships that could have appeared to influence the work reported in this paper.

Acknowledgements

We thank laboratory managers Andrew Hobson and Stephen Reid, and laboratory technician Fiona Key (University of Leeds) for laboratory support. This research project has received funding from the European Research Council (ERC) under the European Union's Horizon 2020 research and innovation programme (Grant agreement No. 725613 MinOrg). A. O. F. and C. L. P. gratefully acknowledge NERC Highlight Topic Grant (NE/S004963/1 Locked Up). Y. Z. gratefully acknowledges support from the China Scholarship Council. C. L. P. gratefully acknowledges Royal Society Wolfson Research Merit Award (WRM/FT/170005).

Appendix A. Supplementary material

Supplementary material to this article can be found online at <https://doi.org/10.1016/j.gca.2022.07.003>.

References

- Adhikari, D., Zhao, Q., Das, K., Mejia, J., Huang, R., Wang, X., Poulson, S.R., Tang, Y., Roden, E.E., Yang, Y., 2017. Dynamics of ferrihydrite-bound organic carbon during microbial Fe reduction. *Geochim. Cosmochim. Acta* 212, 221–233.
- Amstaetter, K., Borch, T., Kappler, A., 2012. Influence of humic acid imposed changes of ferrihydrite aggregation on microbial Fe(III) reduction. *Geochim. Cosmochim. Acta* 85, 326–341.
- Bhattacharyya, A., Schmidt, M.P., Stavitski, E., Azimzadeh, B., Martínez, C.E., 2019. Ligands representing important functional groups of natural organic matter facilitate Fe redox transformations and resulting binding environments. *Geochim. Cosmochim. Acta* 251, 157–175.
- Boily, J.-F., Persson, P., Sjöberg, S., 2000. Benzenecarboxylate surface complexation at the goethite (α -FeOOH)/water interface: II. Linking IR spectroscopic observations to mechanistic surface complexation models for phthalate, trimellitate, and pyromellitate. *Geochim. Cosmochim. Acta* 64, 3453–3470.
- Bradbury, M.H., Baeyens, B., 1999. Modelling the sorption of Zn and Ni on Ca-montmorillonite. *Geochim. Cosmochim. Acta* 63, 325–336.
- Burdige, D.J., 2007. Preservation of Organic Matter in Marine Sediments: Controls, Mechanisms, and an Imbalance in Sediment Organic Carbon Budgets? *Chem. Rev.* 107, 467–485.
- Canfield, D.E., Jørgensen, B.B., Fossing, H., Glud, R., Gundersen, J., Ramsing, N.B., Thamdrup, B., Hansen, J.W., Nielsen, L.P., Hall, P.O., 1993. Pathways of organic carbon oxidation in three continental margin sediments. *Mar. Geol.* 113, 27–40.
- Chen, C., Dynes, J.J., Wang, J., Sparks, D.L., 2014. Properties of Fe-Organic Matter Associations via Coprecipitation versus Adsorption. *Environ. Sci. Technol.* 48, 13751–13759.
- Chen, C., Kukkadapu, R., Sparks, D.L., 2015. Influence of Coprecipitated Organic Matter on Fe²⁺(aq)-Catalyzed Transformation of Ferrihydrite: Implications for Carbon Dynamics. *Environ. Sci. Technol.* 49, 10927–10936.
- Chen, C., Hall, S.J., Coward, E., Thompson, A., 2020. Iron-mediated organic matter decomposition in humid soils can counteract protection. *Nat. Commun.* 11, 1–11.
- Chorover, J., Amistadi, M.K., 2001. Reaction of forest floor organic matter at goethite, birnessite and smectite surfaces. *Geochim. Cosmochim. Acta* 65, 95–109.
- Cornell, R.M., 1985. Effect of Simple Sugars on the Alkaline Transformation of Ferrihydrite into Goethite and Hematite. *Clays Clay Miner.* 33, 219–227.
- Cornell, R.M., Schindler, P.W., 1980. Infrared study of the adsorption of hydroxycarboxylic acids on α -FeOOH and amorphous Fe(III)hydroxide. *Colloid Polym. Sci.* 258, 1171–1175.
- Cornell, R., Schwertmann, U., 1979. Influence of organic anions on the crystallization of ferrihydrite. *Clays Clay Miner.* 27, 402–410.
- Cornell, R.M., Schwertmann, U., 2003. The iron oxides: structure, properties, reactions, occurrences and uses. John Wiley & Sons.
- Cudennec, Y., Lecerf, A., 2006. The transformation of ferrihydrite into goethite or hematite, revisited. *J. Solid State Chem.* 179, 716–722.
- Curti, L., Moore, O.W., Babkhanian, P., Xiao, K.-Q., Wouds, C., Bray, A.W., Fisher, B.J., Kazemian, M., Kaulich, B., Peacock, C.L., 2021. Carboxyl-richness controls organic carbon preservation during coprecipitation with iron (oxyhydr)oxide in the natural environment. *Commun. Earth Environ.* 2, 229.
- Das, S., Hendry, M.J., Essilfie-Dughan, J., 2011. Transformation of Two-Line Ferrihydrite to Goethite and Hematite as a Function of pH and Temperature. *Environ. Sci. Technol.* 45, 268–275.
- Dean, J.A., 1987. *Handbook of Organic Chemistry*. McGraw-Hill Book Co., New York, NY.
- Dobson, K.D., McQuillan, A.J., 1999. In situ infrared spectroscopic analysis of the adsorption of aliphatic carboxylic acids to TiO₂, ZrO₂, Al₂O₃, and Ta₂O₅ from aqueous solutions. *Spectrochim. Acta Part A Mol. Biomol. Spectrosc.* 55, 1395–1405.
- Duckworth, O.W., Martin, S.T., 2001. Surface complexation and dissolution of hematite by C1–C6 dicarboxylic acids at pH = 5.0. *Geochim. Cosmochim. Acta* 65, 4289–4301.
- Eusterhues, K., Rumpel, C., Kögel-Knabner, I., 2005. Organo-mineral associations in sandy acid forest soils: importance of specific surface area, iron oxides and micropores. 56, 753–763.
- Eusterhues, K., Wagner, F.E., Häusler, W., Hanzlik, M., Knicker, H., Totsche, K.U., Kögel-Knabner, I., Schwertmann, U., 2008. Characterization of Ferrihydrite-Soil Organic Matter Coprecipitates by X-ray Diffraction and Mössbauer Spectroscopy. *Environ. Sci. Technol.* 42, 7891–7897.
- Eusterhues, K., Rennert, T., Knicker, H., Kögel-Knabner, I., Totsche, K.U., Schwertmann, U., 2011. Fractionation of Organic Matter Due to Reaction with Ferrihydrite: Coprecipitation versus Adsorption. *Environ. Sci. Technol.* 45, 527–533.
- Eusterhues, K., Hädrich, A., Neidhardt, J., Küsel, K., Keller, T.F., Jandt, K.D., Totsche, K. U., 2014. Reduction of ferrihydrite with adsorbed and coprecipitated organic matter: microbial reduction by *Geobacter bremensis* vs. abiotic reduction by Na-dithionite. *Biogeosciences* 11, 4953–4966.
- Evanko, C.R., Dzombak, D.A., 1999. Surface Complexation Modeling of Organic Acid Sorption to Goethite. *J. Colloid Interface Sci.* 214, 189–206.
- Ford, R.G., Kemner, K.M., Bertsch, P.M., 1999. Influence of sorbate-sorbent interactions on the crystallization kinetics of nickel- and lead-ferrihydrite coprecipitates. *Geochim. Cosmochim. Acta* 63, 39–48.
- Friddle, R.W., Noy, A., De Yoreo, J.J., 2012. Interpreting the widespread nonlinear force spectra of intermolecular bonds. *PNAS* 109, 13573–13578.
- Gu, B., Schmitt, J., Chen, Z., Liang, L., McCarthy, J.F., 1994. Adsorption and desorption of natural organic matter on iron oxide: mechanisms and models. *Environ. Sci. Technol.* 28, 38–46.
- Hall, S.J., Ye, C., Weintraub, S.R., Hockaday, W.C., 2020. Molecular trade-offs in soil organic carbon composition at continental scale. *Nat. Geosci.* 13, 687–692.
- Han, J., Kim, M., Ro, H.-M., 2020. Factors modifying the structural configuration of oxyanions and organic acids adsorbed on iron (hydr)oxides in soils. A review. *Environ. Chem. Lett.* 18, 631–662.
- Han, L., Sun, K., Keiluweit, M., Yang, Y., Jin, J., Sun, H., Wu, F., Xing, B., 2019. Mobilization of ferrihydrite-associated organic carbon during Fe reduction: Adsorption versus coprecipitation. *Chem. Geol.* 503, 61–68.
- Hatcher, P.G., Spiker, E.C., Szeverenyi, N.M., Maciel, G.E., 1983. Selective preservation and origin of petroleum-forming aquatic kerogen. *Nature* 305, 498–501.
- Hedges, J.L., Cowie, G.L., Ertel, J.R., James Barbour, R., Hatcher, P.G., 1985. Degradation of carbohydrates and lignins in buried woods. *Geochim. Cosmochim. Acta* 49, 701–711.
- Hemingway, J.D., Rothman, D.H., Grant, K.E., Rosengard, S.Z., Eglinton, T.I., Derry, L. A., Galy, V.V., 2019. Mineral protection regulates long-term global preservation of natural organic carbon. *Nature* 570, 228–231.
- Henneberry, Y.K., Kraus, T.E.C., Nico, P.S., Horwath, W.R., 2012. Structural stability of coprecipitated natural organic matter and ferric iron under reducing conditions. *Org. Geochem.* 48, 81–89.
- Hiemstra, T., 2013. Surface and mineral structure of ferrihydrite. *Geochim. Cosmochim. Acta* 105, 316–325.
- Hiemstra, T., Van Riemsdijk, W.H., 2009. A surface structural model for ferrihydrite I: Sites related to primary charge, molar mass, and mass density. *Geochim. Cosmochim. Acta* 73, 4423–4436.
- Hiemstra, T., Van Riemsdijk, W.H., Bolt, G.H., 1989. Multisite proton adsorption modeling at the solid/solution interface of (hydr)oxides: A new approach: I. Model description and evaluation of intrinsic reaction constants. *J. Colloid Interface Sci.* 133, 91–104.
- Hiemstra, T., Venema, P., Riemsdijk, W.H.V., 1996. Intrinsic Proton Affinity of Reactive Surface Groups of Metal (Hydr)oxides: The Bond Valence Principle. *J. Colloid Interface Sci.* 184, 680–692.
- Hu, S., Lu, Y., Peng, L., Wang, P., Zhu, M., Dohnalkova, A.C., Chen, H., Lin, Z., Dang, Z., Shi, Z., 2018. Coupled Kinetics of Ferrihydrite Transformation and As(V) Sequestration under the Effect of Humic Acids: A Mechanistic and Quantitative Study. *Environ. Sci. Technol.*
- Hu, S., Liang, Y., Liu, T., Li, F., Lu, Y., Shi, Z., 2020. Kinetics of As(V) and carbon sequestration during Fe(II)-induced transformation of ferrihydrite-As(V)-fulvic acid coprecipitates. *Geochim. Cosmochim. Acta* 272, 160–176.
- Illés, E., Tombác, E., 2006. The effect of humic acid adsorption on pH-dependent surface charging and aggregation of magnetite nanoparticles. *J. Colloid Interface Sci.* 295, 115–123.
- Jelavić, S., Mitchell, A.C., Sand, K.K., 2020. Fate of organic compounds during transformation of ferrihydrite in iron formations. *Geochem. Perspect. Lett.* 15, 25–29.
- Jiang, J., Kappler, A.J., 2008. Kinetics of microbial and chemical reduction of humic substances: implications for electron shuttling. *Environ. Sci. Technol.* 42, 3563–3569.
- Jobbágy, E.G., Jackson, R.B., 2000. The vertical distribution of soil organic carbon and its relation to climate and vegetation. *Ecol. Appl.* 10, 423–436.
- Kaiser, K., Guggenberger, 2003. Mineral surfaces and soil organic matter. *Eur. J. Soil Sci.* 54, 219–236.
- Kaiser, K., Guggenberger, G., 2000. The role of DOM sorption to mineral surfaces in the preservation of organic matter in soils. *Org. Geochem.* 31, 711–725.
- Kaiser, K., Guggenberger, G., 2007. Sorptive stabilization of organic matter by microporous goethite: sorption into small pores vs. surface complexation. *Eur. J. Soil Sci.* 58, 45–59.
- Kaiser, K., Guggenberger, G., Haumaier, L., Zech, W., 1997. Dissolved organic matter sorption on subsoils and minerals studied by ¹³C-NMR and DRIFT spectroscopy. *Eur. J. Soil Sci.* 48, 301–310.
- Kellerman, A.M., Kothawala, D.N., Dittmar, T., Tranvik, L.J., 2015. Persistence of dissolved organic matter in lakes related to its molecular characteristics. *Nat. Geosci.* 8, 454–457.
- Kramer, M.G., Sanderman, J., Chadwick, O.A., Chorover, J., Vitousek, P.M., 2012. Long-term carbon storage through retention of dissolved aromatic acids by reactive particles in soil. *Glob. Change Biol.* 18, 2594–2605.
- Lalonde, K., Mucci, A., Ouellet, A., Gélinas, Y., 2012. Preservation of organic matter in sediments promoted by iron. *Nature* 483, 198.
- Larsen, O., Postma, D., 2001. Kinetics of reductive bulk dissolution of lepidocrocite, ferrihydrite, and goethite. *Geochim. Cosmochim. Acta* 65, 1367–1379.
- Lehmann, J., Kleber, M., 2015. The contentious nature of soil organic matter. *Nature* 528, 60–68.
- Li, Y., Shahbaz, M., Zhu, Z., Chen, A., Nannipieri, P., Li, B., Deng, Y., Wu, J., Ge, T., 2020. Contrasting response of organic carbon mineralisation to iron oxide addition under conditions of low and high microbial biomass in anoxic paddy soil. *Biol. Fertil. Soils*.

- Lindgren, M., Loring, J.S., Persson, P., 2009. Molecular structures of citrate and tricarballoylate adsorbed on alpha-FeOOH particles in aqueous suspensions. *Langmuir* 25, 10639–10647.
- Lovley, D.R., Coates, J.D., Blunt-Harris, E.L., Phillips, E.J., Woodward, J.C., 1996. Humic substances as electron acceptors for microbial respiration. *Nature* 382, 445–448.
- Lu, Y., Hu, S., Wang, Z., Ding, Y., Lu, G., Lin, Z., Dang, Z., Shi, Z., 2019. Ferrihydrite transformation under the impact of humic acid and Pb: kinetics, nanoscale mechanisms, and implications for C and Pb dynamics. *Environ. Sci. Nano* 6, 747–762.
- Lv, J., Zhang, S., Wang, S., Luo, L., Cao, D., Christie, P., 2016. Molecular-Scale Investigation with ESI-FT-ICR-MS on Fractionation of Dissolved Organic Matter Induced by Adsorption on Iron Oxhydroxides. *Environ. Sci. Technol.* 50, 2328–2336.
- Mayer, L.M., 1999. Extent of coverage of mineral surfaces by organic matter in marine sediments. *Geochim. Cosmochim. Acta* 63, 207–215.
- McCullom, T.M., Seewald, J.S., 2003. Experimental study of the hydrothermal reactivity of organic acids and acid anions: II. Acetic acid, acetate, and valeric acid. *Geochim. Cosmochim. Acta* 67, 3645–3664.
- Mesuer, K., Fish, W., 1992a. Chromate and oxalate adsorption on goethite. 1. Calibration of surface complexation models. *Environ. Sci. Technol.* 26, 2357–2364.
- Mesuer, K., Fish, W., 1992b. Chromate and oxalate adsorption on goethite. 2. Surface complexation modeling of competitive adsorption. *Environ. Sci. Technol.* 26, 2365–2370.
- Michel, F.M., Ehm, L., Liu, G., Han, W.Q., Antao, S.M., Chupas, P.J., Lee, P.L., Knorr, K., Eulert, H., Kim, J., Grey, C.P., Celestian, A.J., Gillow, J., Schoonen, M.A.A., Strongin, D.R., Parise, J.B., 2007. Similarities in 2- and 6-Line Ferrihydrite Based on Pair Distribution Function Analysis of X-ray Total Scattering. *Chem. Mater.* 19, 1489–1496.
- Mikutta, R., Kleber, M., Torn, M.S., Jahn, R., 2006. Stabilization of Soil Organic Matter: Association with Minerals or Chemical Recalcitrance? *Biogeochemistry* 77, 25–56.
- Moon, Ellen M., Peacock L., Caroline L., 2013. Modelling Cu(II) adsorption to ferrihydrite and ferrihydrite–bacteria composites: Deviation from additive adsorption in the composite sorption system. *Geochim. Cosmochim. Acta* 104, 148–164.
- Newcomb, C.J., Qafoku, N.P., Grate, J.W., Bailey, V.L., De Yoreo, J.J., 2017. Developing a molecular picture of soil organic matter–mineral interactions by quantifying organo–mineral binding. *Nat. Commun.* 8, 396.
- Peacock, C.L., Sherman, D.M., 2004. Copper(II) sorption onto goethite, hematite and lepidocrocite: a surface complexation model based on ab initio molecular geometries and EXAFS spectroscopy. *Geochim. Cosmochim. Acta* 68, 2623–2637.
- Poggenburg, C., Mikutta, R., Sander, M., Schippers, A., Marchanka, A., Dohrmann, R., Guggenberger, G., 2016. Microbial reduction of ferrihydrite-organic matter coprecipitates by *Shewanella putrefaciens* and *Geobacter metallireducens* in comparison to mediated electrochemical reduction. *Chem. Geol.* 447, 133–147.
- Ravel, B., Newville, M., 2005. ATHENA, ARTEMIS, HEPHAESTUS: data analysis for X-ray absorption spectroscopy using IFEFFIT. *J. Synchrotron Radiat.* 12, 537–547.
- Reddy, T.R., Frierdich, A.J., Beard, B.L., Johnson, C.M., 2015. The effect of pH on stable iron isotope exchange and fractionation between aqueous Fe(II) and goethite. *Chem. Geol.* 397, 118–127.
- Rothe, J., Denecke, M.A., Dardenne, K., 2000. Soft X-Ray Spectromicroscopy Investigation of the Interaction of Aquatic Humic Acid and Clay Colloids. *J. Colloid Interface Sci.* 231, 91–97.
- Rothman, D.H., Forney, D.C., 2007. Physical Model for the Decay and Preservation of Marine Organic Carbon. *Science* 316, 1325.
- Rowley, M.C., Grand, S., Verrecchia, É.P., 2017. Calcium-mediated stabilisation of soil organic carbon. *Biogeochemistry* 137, 27–49.
- Ruddiman, W.F., 2001. *Earth's Climate: Past, Present and Future*. W.H. Freeman, New York.
- Sakakibara, M., Tanaka, M., Takahashi, Y., Murakami, T., 2019. Redistribution of Zn during transformation of ferrihydrite: Effects of initial Zn concentration. *Chem. Geol.* 522, 121–134.
- Schmidt, M.W., Torn, M.S., Abiven, S., Dittmar, T., Guggenberger, G., Janssens, I.A., Kleber, M., Kögel-Knabner, I., Lehmann, J., Manning, D.A., Nannipieri, P., Rasse, D.P., Weiner, S., Trumbore, S.E., 2011. Persistence of soil organic matter as an ecosystem property. *Nature* 478, 49–56.
- Schwertmann, U., Cornell, R.M., 2000. *Iron Oxides in the Laboratory: Preparation and Characterization*, second. Wiley-VCH, Weinheim, Germany.
- Schwertmann, U., Fischer, W., 1966. Zur Bildung von α -FeOOH und α -Fe₂O₃ aus amorphem Eisen (III)-hydroxid. III. *Zeitschrift für anorganische und allgemeine Chemie* 346, 137–142.
- Sherman, D.M., Peacock, C.L., Hubbard, C.G., 2008. Surface complexation of U(VI) on goethite (α -FeOOH). *Geochim. Cosmochim. Acta* 72, 298–310.
- Six, J., Conant, R.T., Paul, E.A., Paustian, K., 2002. Stabilization mechanisms of soil organic matter: Implications for C-saturation of soils. *Plant Soil* 241, 155–176.
- Solomon, D., Lehmann, J., Kinyangi, J., Liang, B., Schäfer, T., 2005. Carbon K-Edge NEXAFS and FTIR-ATR Spectroscopic Investigation of Organic Carbon Speciation in Soils. *Soil Sci. Soc. Am. J.* 69, 107–119.
- Sparks, D.L., 2003. *Environmental soil chemistry*. Elsevier.
- Sposito, G., 2008. *The chemistry of soils*. Oxford University Press.
- Torn, M.S., Trumbore, S.E., Chadwick, O.A., Vitousek, P.M., Hendricks, D.M., 1997. Mineral control of soil organic carbon storage and turnover. *Nature* 389, 170–173.
- Vogel, C., Mueller, C.W., Höschel, C., Buegger, F., Heister, K., Schulz, S., Schlöter, M., Kögel-Knabner, I., 2014. Submicron structures provide preferential spots for carbon and nitrogen sequestration in soils. *Nat. Commun.* 5, 2947.
- Wagai, R., Mayer, L.M., 2007. Sorptive stabilization of organic matter in soils by hydrous iron oxides. *Geochim. Cosmochim. Acta* 71, 25–35.
- Wang, S., Lei, L., Zhang, D., Zhang, G., Cao, R., Wang, X., Lin, J., Jia, Y., 2020. Stabilization and transformation of selenium during the Fe(II)-induced transformation of Se(IV)-adsorbed ferrihydrite under anaerobic conditions. *J. Hazard. Mater.* 384.
- Wershaw, R.L., 1994. Membrane-micelle model for humus in soils and sediments and its relation to humification. *Water Supply Paper*.
- Westall, J., Hohl, H., 1980. A comparison of electrostatic models for the oxide/solution interface. *Adv. Colloid Interface Sci.* 12, 265–294.
- Zeng, Q., Huang, L., Ma, J., Zhu, Z., He, C., Shi, Q., Liu, W., Wang, X., Xia, Q., Dong, H., 2020. Bio-reduction of ferrihydrite-montmorillonite-organic matter complexes: Effect of montmorillonite and fate of organic matter. *Geochim. Cosmochim. Acta* 276, 327–344.
- Zhao, Q., Poulson, S.R., Obrist, D., Sumaila, S., Dynes, J.J., McBeth, J.M., Yang, Y., 2016. Iron-bound organic carbon in forest soils: quantification and characterization. *Biogeochemistry* 13, 4777–4788.